Dynamic Multiscale Modes of Severe Storm Structure Detected in Mobile Doppler Radar Data by Entropy Field Decomposition

LAWRENCE R. FRANK

Center for Scientific Computation in Imaging, University of California, San Diego, La Jolla, California

VITALY L. GALINSKY

Center for Scientific Computation in Imaging, and Electrical and Computer Engineering Department, University of California, San Diego, La Jolla, California

LEIGH ORF

Cooperative Institute for Meteorological Satellite Studies, University of Wisconsin–Madison, Madison, Wisconsin

JOSHUA WURMAN

Center for Severe Weather Research, Boulder, Colorado

(Manuscript received 14 April 2017, in final form 20 November 2017)

ABSTRACT

The detection of complex spatially and temporally varying coherent structures in data from highly nonlinear and non-Gaussian systems is a challenging problem in a wide range of scientific disciplines. This is the case in the analysis of Doppler on Wheels (DOW) mobile Doppler radar (MDR) data where the goal is to detect rapidly evolving coherent storm structures that reflect the complex interplay of nonlinear dynamical processes. Estimating and quantifying such structures from the noisy and relatively sparsely sampled MDR data poses a difficult inverse problem for which traditional analysis methods such as expert and subjective pattern recognition, thresholding, and contouring choices can be difficult. In this paper the authors investigate the application of a recently developed objective method for the analysis of spatiotemporal data called the entropy field decomposition (EFD) to the problem of the analysis of MDR data in tornadic supercells. The EFD method is based on a field theoretic reformulation of Bayesian probability theory that incorporates prior information from the coupling structure within the data to automatically detect multivariate spatiotemporal modes. The method is first applied to data from a numerically simulated tornadic supercell in order to validate the method's ability to detect and quantify known storm-scale features. It is then applied to actual MDR data collected during the evolution of a tornadic supercell—data that have been analyzed previously by experts. The authors demonstrate the ability of the EFD method to detect spatiotemporal features currently believed to be related to tornadogenesis. This new method has the potential to provide improved and objective analysis/detection with increased sensitivity to nonlinear and non-Gaussian spatially and temporally coherent features related to tornadogenesis and thus offers the potential to aid in the study, prediction, and warnings of tornadoes.

1. Introduction

The mechanisms by which tornadoes are formed within supercell thunderstorms (tornadogenesis) remain a significant scientific mystery. This is a problem of both great scientific interest and social impact, as the ability to understand tornado formation is critical in reducing the time between issuing of tornado warnings to potentially affected populations and tornado formation. However, the interplay of spatiotemporally varying processes within the highly dynamic supercell environment that result in the formation of tornadoes is much too complex to lend itself to analytical modeling, leaving essentially two methods as viable approaches to addressing this problem: numerical simulation (e.g., Klemp and Rotunno 1983; Rotunno and Klemp 1985; Wicker and Wilhelmson 1995; Adlerman et al. 1999; Markowski et al. 2003; Markowski and Richardson 2014;

Corresponding author: Lawrence R. Frank, lfrank@ucsd.edu

DOI: 10.1175/JAS-D-17-0117.1

Orf et al. 2017) and observational methods, such as Doppler radar and in situ observations (e.g., Brandes 1978, 1984; Dowell and Bluestein 1997; Wakimoto and Cai 2000; Wakimoto et al. 2011, 2012; Trapp 1999; Dowell and Bluestein 2002a,b; Markowski et al. 2002; Beck et al. 2006; Wurman et al. 2007b,a,c; Grzych et al. 2007; Marquis et al. 2008; Wurman et al. 2010; Atkins et al. 2012; Marquis et al. 2012; Markowski et al. 2012a,b; Kosiba et al. 2013; Kosiba and Wurman 2013; Wurman and Kosiba 2013; Wurman et al. 2014). Both of these approaches present their own tremendous technical challenges that have nonetheless been met with a long history of innovative research that leverages significant advances in both computational capabilities and radar hardware to bring an increasingly deep understanding of tornadogenesis.

However, while computational modeling (e.g., simulation) and observational experiments [e.g., the Doppler on Wheels (DOW) (Wurman et al. 1997) and other mobile Doppler radar (MDR) systems] are essential tools of any comprehensive program aimed at understanding tornadogenesis, so is a robust and accurate quantitative approach for estimating coherent spatiotemporal features within these highly nonlinear and non-Gaussian multivariate data, whether real or simulated. As numerical simulations become increasingly capable of recreating tornadogenesis using realistic physical models there becomes a greater need for sophisticated analysis methods that can characterize the resulting nonlinear and non-Gaussian multivariate spatiotemporal patterns, or modes, of severe convective storms. More accurate and objective analysis methods for data acquired in these nonlinear systems and contaminated with non-Gaussian noise are necessary to provide robust comparisons with both simulated storms and with theoretical predictions. With this increased accuracy comes the ultimate goal of a better understanding of the mechanisms of tornadogenesis as well as the possibility of more accurate prediction and subsequent warning of tornadic events.

To address this type of problem, we have recently developed a new general approach to the analysis of spatiotemporal data called the entropy field decomposition (EFD) (Frank and Galinsky 2016a,b), which combines information field theory (IFT) (Enßlin et al. 2009) with prior information encoded on spatiotemporal patterns using our recently introduced method of entropy spectrum pathways (ESP) (Frank and Galinsky 2014). The formulation of this method is quite general and can be applied to any form of time-varying multivariate volumetric data, a point emphasized by our initial demonstration of the general theory (Frank and Galinsky 2016b) on both functional magnetic resonance imaging (FMRI) data and dual-Doppler radar data collected by a DOW MDR (Wurman et al. 1997; Wurman 2001) during the genesis and intensification of the Goshen County, Wyoming, tornado on 5 June 2009 observed in the Second Verification of the Origins of Tornadoes Experiment (VORTEX2) (Wurman et al. 2012; Kosiba et al. 2013).

The purpose of the current paper is to apply the EFD method to both simulated and real data from severe convective storms in order to assess its capability of detecting complex spatiotemporal patterns of parameters (e.g., vorticity) that might inform our understanding of tornadogenesis. In other words, are there certain physical and/or kinematic configurations of supercells that are associated with tornadogenesis more often than others?

In addition to refining our previous analysis of the Goshen data (Frank and Galinsky 2016a), we study the application of the EFD method in a numerically simulated tornadic supercell (Orf et al. 2017), which provides the opportunity for validating the method. We demonstrate that our method is both automated and quantitative and provides an analysis approach sensitive to coherent multivariate features produced by the complex nonlinear dynamical processes in severe convective storms. It thus offers the potential to augment current theoretical, numerical, and experimental studies of tornadogenesis and may ultimately prove suitable for use with operational weather radar networks deployed in the service of protecting the public.

2. Overview of EFD

a. General formulation

The primary objective of a wide range of data analysis problems can be expressed as the desire to estimate unknown quantities s from the data d using available prior information I that one might have about the problem. For imaging systems, the data d may include complex spatiotemporal dependencies; for example, it may be a single value (intensity) recorded for every spatial location, a multiple-value vector or tensor field data, or a time sequence of values (or a combination of different types). For example, MDR systems collect data that are volumetric time series of both reflectivity intensity and velocity vector measurements. So generally any single point in such a dataset d is a spatiotemporal point—that is, a location in space–time. From Bayes theorem, the posteriori distribution for any of the unknowns can be expressed as

$$\underbrace{p(s|d,I)}_{\text{Posterior}} = \frac{\overbrace{p(d,s|I)}^{\text{Joint probability}}}{\underbrace{p(d|I)}_{\text{Evidence}}} = \frac{\overbrace{p(d|s,I)}^{\text{Likelihood}}\overbrace{p(s|I)}^{\text{Prior}}}{p(d|I)} \quad \text{and} \tag{1a}$$

$$p(d|I) = \int ds\, p(d,s|I). \quad (1b)$$

The IFT (Enßlin et al. 2009) uses the formalism of field theory and expresses the terms in Eq. (1a) using an information Hamiltonian $H(d, s)$ as

$$H(d,s) = -\ln p(d,s|I) \quad \text{(Hamiltonian)} \quad \text{and} \quad (2a)$$

$$p(d|I) = \int ds\, e^{H(d,s)} = Z(d) \quad \text{(Partition function)} \quad (2b)$$

so that the posterior distribution Eq. (1a) becomes

$$p(s|d,I) = \frac{e^{-H(d,s)}}{Z(d)}. \quad (3a)$$

The formulation of probability theory (i.e., Bayes theorem) in terms of field theory via Eq. (3a) is useful because it facilitates the use of all the well-known mathematical machinery of field theory for describing arbitrarily complicated approximations of nonlinear and non-Gaussian interacting fields (e.g., Ryder 1985). However, from a practical perspective this formulation provides no guidance on how to work with an arbitrarily large parameter space and the subsequently huge number of nonlinear interacting terms that would be typical of actual data such as that acquired in MDR. The essence of the EFD approach (Frank and Galinsky 2016a,b) is the recognition that the parameter space of system configurations that are consistent with the data can be identified using the ESP theory (Frank and Galinsky 2014) and that the number of these configurations turns out to be actually quite limited and amenable to efficient and robust computation. Consequently, even large, multivariate datasets from complex nonlinear and non-Gaussian physical systems (such as severe storms or the human brain) can be described by a reasonable number of field configurations, or modes, that can characterize the system (Frank and Galinsky 2016a,b).

This identification of consistent parameter configurations occurs as a consequence of the main result of the ESP theory: A coupling matrix Q_{ij} is constructed from the data that characterize the relation between space–time locations ξ_i and ξ_j in the data ($\boldsymbol{\xi} \equiv \{\mathbf{x}, t\}$), and the spectrum of the coupling matrix eigenvalues determines the most probable configuration of parameters, which are described by the associated eigenvectors. From a probabilistic standpoint, the coupling can be viewed as prior information that is contained within the data and whose spectrum constrains the resulting posterior distribution of the parameters (Frank and Galinsky 2014).

So how is this coupling matrix constructed? One of the powerful features of the ESP approach is that the coupling matrix can be arbitrarily constructed by the user from the data depending on the problem at hand. While this choice is arbitrary, its use is not: once the coupling matrix has been defined, the ESP theory, and by extension the EFD formalism, then has a precise method for incorporating it. Consider the simplest case in which the coupling matrix is constructed assuming data at space–time points $d(\xi_i)$ only interact if i and j are nearest neighbors ($|i - j| = 1$) and that each neighbor is chosen to be either completely connected to the data at space–time location j, in which case $Q_{ij} = 1$, or completely unconnected, in which case $Q_{ij} = 0$. In this special case, Q_{ij} is then just the adjacency matrix.

But in practical applications, such as the present case, the coupling matrix Q_{ij} is more generally defined in terms of continuous values derived from some more complex model of interactions and not necessarily just between nearest neighbors. For example, one might consider a velocity vector field $\mathbf{v}(x)$ and define the coupling matrix as proportional to the angle between the vectors [e.g., $Q_{ij} = \mathbf{v}(x_i) \cdot \mathbf{v}(x_j)$] and then solve the problem for i and j as nearest neighbors, next-nearest neighbors, etc., to explore spatiotemporal patterns at different spatiotemporal scales. In the present paper we will show that even simple coupling strategies produce useful results. However, it is anticipated that future work will involve the inclusion of coupling models based on more complex models of storm dynamics.

The full details of the mathematical formulation of EFD can be found in Frank and Galinsky (2016a,b) but a briefer introduction can be found in the appendix below.

b. *Space–time tractography*

The general nature of the EFD facilitates further analysis that has the potential to provide more detailed information on the nature of dynamic storm processes. The general EFD framework constructs the modes from spatiotemporal patterns in parameters that are generally tensorial in nature. A useful feature of EFD with tensorial parameters is its ability to construct long-range space–time correlations through the generation of spatially continuous parameter pathways, or tracts, by the incorporation of our recently developed tractography method, which employs a geometrical optics approach guided by ESP (GO-ESP; Galinsky and Frank 2015). Although this approach was developed in the context of mapping neural pathways from diffusion-weighted MRI data, the method actually makes no assumption about the type of data and can be viewed as a general procedure for constructing the optimal estimates of the space–time trajectories traversed by system parameters. We call this general procedure space–time tractography and refer to the resulting pathways as space–time tracts.

These tracts provide additional information about the detected modes that is not directly apparent from the modes themselves but is embedded in the estimated spatiotemporal patterns.

One possible way to implement this general principle is to define a Hamiltonian $\mathscr{H}_m(\mathbf{x}, \mathbf{k})$ as the averaged temporal correlation function of the space–time signal

$$\mathscr{H}_m(\mathbf{x}, \mathbf{k}) = \frac{1}{T} \int\int s_m(\mathbf{x}, t') s_m(\mathbf{x} + \mathbf{k}, t' + t)\, dt\, dt', \quad (4)$$

where $s_m(\mathbf{x}, t)$ is the mth mode signal and $T = t_n - t_1$. Then the trajectory is integrated starting from a seed point to follow the maximum correlation with

$$\frac{d\mathbf{x}}{dt} = \frac{\partial \mathscr{H}_m}{\partial \mathbf{k}} \quad \text{and} \quad \frac{d\mathbf{k}}{dt} = -\frac{\partial \mathscr{H}_m}{\partial \mathbf{x}}, \quad (5)$$

where $\mathbf{k}$ is the conjugate variable of the spatial coordinate $\mathbf{x}$ (i.e., the momentum). Tracts are then constructed from the space–time trajectory of the maximum correlations. In practice, the computation of $\mathscr{H}_m(\mathbf{x}, \mathbf{k})$ comes essentially "for free" in that the temporal pair correlation function is already computed as part of the EFD processing scheme. From a practical perspective, the most straightforward implementation of tractography is to assume that tracts traverse the high-probability regions of the parameters estimated using the EFD procedure outlined above, using the probability surfaces of the ranked modes as seed points.

Tractography results produce a multitude of pathways that can be difficult to interpret or categorize in a succinct fashion. A useful quantitative characterization of the paths can be constructed from the eigenmodes of the connectivity matrix generated from all of the starting and ending points of each tract (Frank and Galinsky 2016a,b). These are called space–time tract eigenmodes and represent the trajectory of maximum space–time correlation within a given mode. These eigenmodes can be ranked according to their associated eigenvalues. The principal eigenmode is thus the one associated with the largest eigenvalue and interpreted as the primary, or most probable, pathway in the data. The significance of these eigenmodes to the dynamical processes such as tornadogenesis is an interesting question that will be explored in future work.

3. Implementation

The general EFD formalism is very flexible and allows for multiple spatial and temporal correlation orders to be incorporated and can include a wide range of prior information. The procedure used in this paper for estimating the signal modes consisted of the following steps:

1) Generate a coupling matrix for data d at the space–time locations $\boldsymbol{\xi} \equiv \{\mathbf{x}, t\}$ as $Q(\xi_i, \xi_j) = d(\xi_i)d(\xi_j)A_{ij}$, where $d(\xi_i)d(\xi_j)$ may represent either the product of two scalars, or the dot product of vectors or tensors, and A_{ij} characterizes whether two space–time locations are connected or not. For example, for simple nearest neighbor coupling, $\mathbf{A}$ is just the space–time adjacency matrix: A_{ij} equals 1 if i and j are nearest neighbors in space or time domains and 0 otherwise. Multiple spatial and temporal scale modes are generated by extending the space–time correlation lengths in $\mathbf{A}$.
2) Find ESP eigenvalues λ_k and eigenvectors $\boldsymbol{\phi}^{(k)}$ for the coupling matrix $Q(\xi_i, \xi_j)$ by solving the eigenvalue problem in Eq. (A5).
3) Use ESP eigenvalues λ_k and eigenvectors $\boldsymbol{\phi}^{(k)}$ to construct the information Hamiltonian [Eq. (A10)], where $\boldsymbol{\Lambda}$ is simply the diagonal matrix $\mathrm{Diag}\{\lambda_1, \ldots, \lambda_K\}$ of ESP eigenvalues and the interaction terms $\boldsymbol{\Lambda}^{(n)}$ are constructed from ESP eigenvalues and eigenvectors with the help of Eq. (A12).
4) Finally, the amplitudes a_k that describe both spatially and temporally interacting modes of the information Hamiltonian [Eq. (A10)] are found from the nonlinear expression for the classical solution [Eq. (A15)].

The procedure above uses a complete spatial–temporal ESP basis for the signal expansion [Eq. (A9)]. We note that it is also possible to formulate the ESP method using a Fourier expansion in the temporal domain. This approach is useful when the data are densely sampled in time (Frank and Galinsky 2016b) but is less advantageous for data irregularly and sparsely sampled in time, such as the DOW data used in this paper. However, simulation data would be amenable to this formulation. We anticipate that the Fourier method will be useful in the future as improvements are made in MDR systems that facilitate more rapid sampling.

All the algorithms implemented in this paper were written in standard ANSI C/C++ and parallelized using POSIX threads, resulting in an efficient computational implementation. For example, estimation of reflectivity (dBZ) modes for all 12 combinations of 3 temporal and 4 spatial scales on the 13-GB simulation data of size $(n_x, n_y, n_z, n_t) = (240, 240, 80, 37)$ took approximately 41 min on a dual E5-2697 v3 2.6-GHz 14-core 145-W Linux machine with 512 GB DDR4 EEC registered memory. Tractography for any particular dBZ mode took approximately 6 min.

We would like to emphasize that the above implementation is but one manifestation of the method. Because the coupling matrix $\mathbf{Q}$ can be constructed in a

variety of ways, and higher-order terms can be included to incorporate more complex interactions between signal and noise components, the method provides the framework to explore a wide range of implementations presumed suitable in different applications. However, the key point is that, while the particular implementations may differ, the logic remains unchanged and is represented by Bayes theorem [Eq. (3a)] with well-defined parameters in the construction of the information Hamiltonian [Eq. (A10)] that must always be explicitly enunciated. In the results shown in this paper no special processing was performed. Aside from the standard preprocessing to the DOW data to remove clutter and regrid to a Cartesian grid (see, e.g., Wurman et al. 2007a), no additional noise reduction, smoothing filters, or other preprocessing steps for dimensionality reduction were performed. It is particularly important to note that the spatial and temporal dimensions are handled in a unified manner as simply different dimensions in a general space–time problem. It is also possible to extend the method to incorporate multiple modalities of data by generalizing the coupling matrix to incorporate coupling between the different modalities. For example, instead of estimating the vorticity EFD modes just from the measured vorticity field, it is also possible to estimate them by coupling the vorticity field to the reflectivity field, if there is a physical model that suggests a relationship between the two such that the reflectivity field provides information that can constrain the estimates of the vorticity modes. The application of this generalization to severe weather data will be the subject of future work.

In the next sections we detail the application of the EFD method to a numerically simulated tornadic supercell (Orf et al. 2017) and to actual MDR data collected by the DOW team (Wurman et al. 2012; Kosiba et al. 2013). Meteorological parameters estimated by EFD will have an ''EFD'' subscript, whereas the corresponding measured (or simulated) meteorological parameter will not. For example, the estimated vertical vorticity will be denoted ζ_{EFD} whereas the measured or simulated quantity will be simply ζ.

The EFD analysis method can be applied to any one of the multitude of multidimensional parameters that characterize tornadic supercells. Presently, we focus on just a few critical parameters: radar reflectivity (dBZ), vorticity ($\boldsymbol{\omega}$), vertical vorticity (ζ), and the stretching term in the vertical vorticity equation (σ). The vertical vorticity $\zeta = \mathbf{k} \cdot (\nabla \times \mathbf{V})$ and stretching of ζ is defined as $\sigma = -\zeta[(\partial u/\partial x) + (\partial v/\partial y)]$. We note that while only the vertical vorticity ζ is analyzed for the DOW data, the full 3D vorticity $\boldsymbol{\omega}$ is available in the simulation data. We therefore use these different quantities in the analysis below. The analysis itself does not change, of course.

4. Application to a simple toy problem

The data from both the numerical simulations and mobile Doppler radar are exceedingly complex and so it is useful to demonstrate the EFD on a much simpler problem. This will help clarify the differences, and advantages, of EFD over more traditional analysis methods such as contouring. For this purpose we have constructed a simple toy model that consists of a modified form of a 3D vortex tube generated with a modified version of Burgers's vortex (Burgers 1948) (i.e., characterized by a Gaussian vorticity profile) in which the center line of the vortex tube is described by an arbitrary curve in space and time. The Burgers's vortex is an exact solution to the Navier–Stokes equations for viscous flow that is easily solved for a straight tube that admits a simple solution when expressed in cylindrical coordinates (e.g., Tryggeson 2007). However, the solution along an arbitrary curve is nontrivial (we are not aware that this has been solved) so, strictly speaking, our construction assumes that the curve bends slowly enough (in space) that Burgers's vortex solution is valid locally (i.e., short lengths of the tube are considered straight cylinders.). Nevertheless, it produces a time-varying tube of Gaussian vorticity (across the tube) that provides a useful model for constructing, testing, and comparing analysis algorithms.

Two Burgers's vortex tubes with identical vorticity profiles across the tube (in the reference frame of the tube) but different sizes and distances from the origin were constructed along helical trajectories in the vertical (z) axis. The tubes were then made to rotate about both a common origin in the x–y plane and about their core axis. Ten time steps were simulated during which time the tubes made one complete rotation about the origin. The data generated in the toy simulation are shown in Fig. 1 (top) where contours of vorticity magnitude are shown. Being of equal vorticity magnitudes, both tubes show up in the same contour plot. One can think of them as being in the same ''contour mode.'' The results of the EFD processing are shown in bottom of Fig. 1. Two EFD modes are detected (colored in blue and red) corresponding to two separate spatiotemporal patterns. These modes are just the two different vortex tubes. So, while the tubes appear together in a contour plot, they are distinguishable by EFD (i.e., appear as different EFD modes) because they do, in fact, have different spatiotemporal structure.

Another aspect of the EFD method is important to point out here. The EFD modes represent probabilities and therefore the displayed surfaces such as those shown in Fig. 1 (bottom) represent surfaces of constant probability. Therefore the numerical values associated with

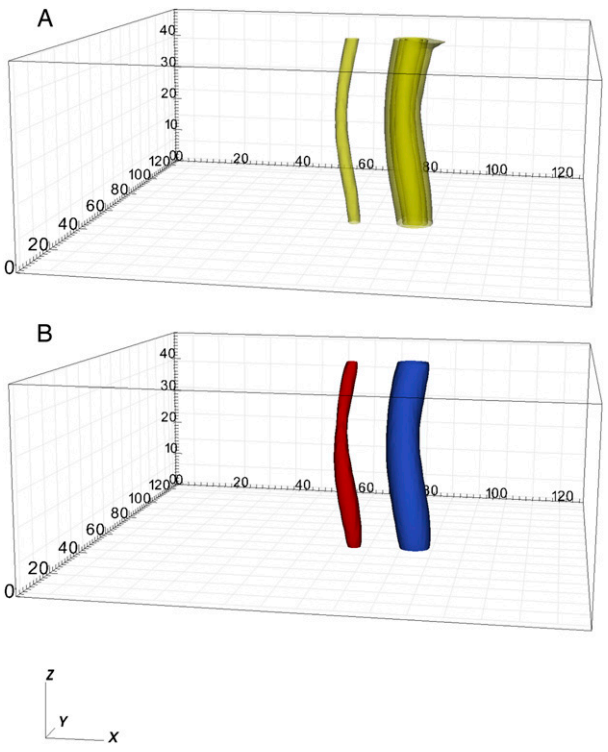

FIG. 1. Toy problem. (a) Two helical Burgers vortex tubes with the same vorticity rotating about a common origin in the x–y plane. A single time frame of the 10 time steps in the data is shown. Contours of vorticity magnitude in the data show both tubes simultaneously. (b) EFD analysis of the data detects two different spatiotemporal modes corresponding to the two different vortex tubes. One mode contains only one tube (red) rotating around the center. The second mode contains the other tube (blue) rotating around the center. This image shows the combined mode at the same time point.

these surfaces are not the values of the parameters being estimated. By construction, the eigenvectors in the EFD formulation from which these modes are constructed (appendix) are of unit magnitude. Multiplication of the eigenvectors by their associated eigenvalue scales them into the same units as the parameter (e.g., vorticity) but that does not guarantee that the value at a particular location in the mode is the same as the corresponding value in the data (and it typically is not). The reason for this is that the eigenmodes are constructed from a mixture of interacting fields in both space and time. However, once a mode is constructed, one can always extract (or display) the parameter values within the high-probability regions of the EFD modes.

This toy problem is admittedly simplistic from a meteorological standpoint but serves to illustrate the meaning of the EFD modes and their fundamental difference from contour plotting.

5. Application to a numerically simulated tornadic supercell

Numerical simulations provide an excellent test bed for the validation of computational estimation methods, as the parameter fields are precisely known. However, modern simulations are themselves so complex that the resultant numerically generated storms are well served by estimation techniques such as EFD in order to identify important complex dynamical features.

a. *Simulation details*

The simulation analyzed was a low-resolution (500-m horizontal and 250-m vertical grid spacing) version of the tornadic supercell described in Orf et al. (2017). This simulation will be referred to as ER500. The sounding used to initialize the CM1 model, release 18 (Bryan and Fritsch 2002), was taken from a 1-h Rapid Update Cycle (RUC) model forecast off the right flank of the storm that was observed to produce the Calumet–El Reno–Piedmont–Guthrie tornado of 24 May 2011 [for a description of the observed storm, refer to Tanamachi et al. (2015), Houser et al. (2015), and French et al. (2015)]. The base-state environment of the simulation was characterized by large amounts of convective available potential energy, large amounts of deep-layer and near-surface vertical wind shear, a low lifted condensation level, and storm-relative helicity values associated with strongly tornadic supercell thunderstorms (Thompson et al. 2003). For a full description of the environmental conditions that initialized CM1, see Orf et al. (2017). Gross features of the 500-m simulation analyzed herein are consistent with those observed in Orf et al. (2017), including a vigorous low-level mesocyclone and tornado-like vortex (TLV) that persists for over one-half hour, producing ground-relative winds exceeding 60 m s^{-1} at the model's lowest grid level, consistent with an EF3 tornado. Further, a feature found just behind the forward-flank downdraft boundary (FFDB), consistent with the streamwise vorticity current (SVC; Orf et al. 2017) is present during the period where the lowest surface pressure (−33 hPa) associated with the tornado-like vortex are found. Thirty-seven model times were saved to history files in 300-s intervals spanning 3 h of model time, and EFD analysis covered all saved times. This is rather coarse sampling for supercells but sufficient to resolve the developing tornado-like vortex. Future studies focused more on the specific mechanisms of tornadogenesis will utilize much higher spatial and temporal resolution simulation data in which much finer spatiotemporal features are evident.

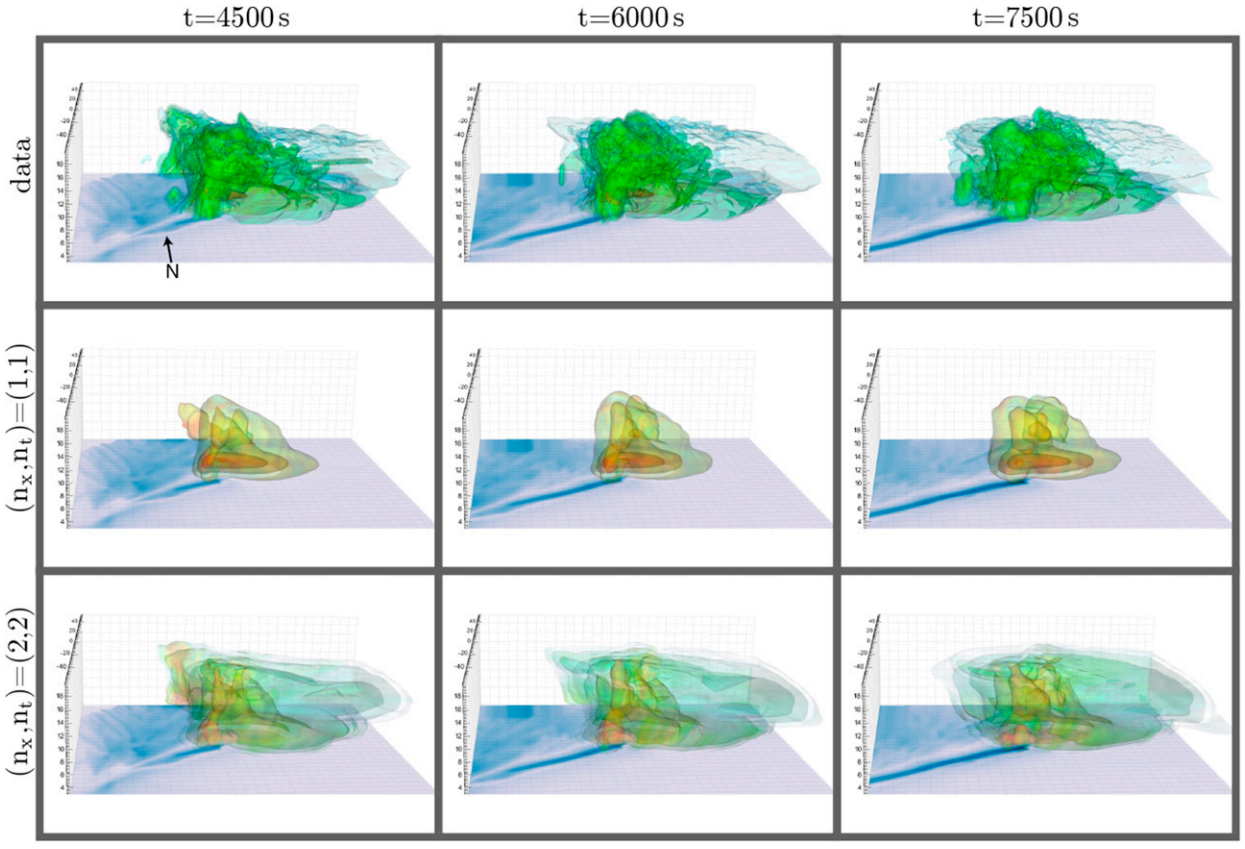

FIG. 2. ER500 analysis of radar reflectivity at three different model times: (left to right) 4500, 6000, and 7500 s. (top) Five equally spaced semitransparent contours of model-calculated reflectivity in the range {0, 60} dBZ. (middle),(bottom) The dBZ_{EFD} modes for $(n_x, n_t) = (1, 1)$ and $(n_x, n_t) = (2, 2)$, respectively, at the same times as in the (top). For the dBZ_{EFD} modes, five contours from 0 to the mode maximum value are shown. EFD contours are shaded by model reflectivity along the contour surface. View is looking toward the north, and the surface pseudocolor field is the maximum surface horizontal wind speed translated with the moving model domain. The dark blue linear feature traces the ground-relative surface path of the TLV. Tick marks are every 4 km. Axes are marked in kilometers.

b. EFD analysis

In Fig. 2, we compare traditional contour analysis of the reflectivity field of ER500 to EFD estimated modes at three different model times. At $t = 4500$ s a plan view of simulated reflectivity at 2 km AGL (not shown) indicates the primary (cyclonic) supercell exhibiting a classic reflectivity signature with reflectivity maxima in the storm's forward flank and a hook echo and weak-echo region. The remnants of a left-moving cell are exiting the model domain's northern boundary at this time, and a region of enhanced reflectivity (~400-km^2 region exhibiting values exceeding 50 dBZ) persists until $t =$ 7500 s. The quantity dB$Z_{\mathrm{EFD}}(1, 1)$ cleanly captures each of the aforementioned physical features, whereas mode dB$Z_{\mathrm{EFD}}(2, 2)$ presents a more complex picture, with the new EFD modes covering a larger volume and exhibiting secondary features not found in dB$Z_{\mathrm{EFD}}(1, 1)$.

In Fig. 3, we explore vertical vorticity stretching, with six model data contours spanning the range $[-1, 1] \times 10^{-3}$ s^{-2} shown in the top row. Focusing on the region in the vicinity of the TLV near the ground, contours indicate a structure with large positive values of stretching maximized immediately above the ground beneath an elevated tube-like region of negative vorticity stretching where minimum values are found approximately 4 km AGL. An exploration of the updraft and vertical vorticity in this region reveals a vigorous low-level mesocyclone with a local updraft maximum centered approximately 3 km AGL. The dipole-like structure of the stretching field can be explained by approximating the cyclonically rotating updraft as an ellipsoid with an updraft maximum at its center, with negative stretching values above the center of the ellipsoid (where $\partial w/\partial z$ is negative) above a region of positive stretching (where $\partial w/\partial z$ is positive). EFD modes $\sigma_{\mathrm{EFD}}(1, 1)$

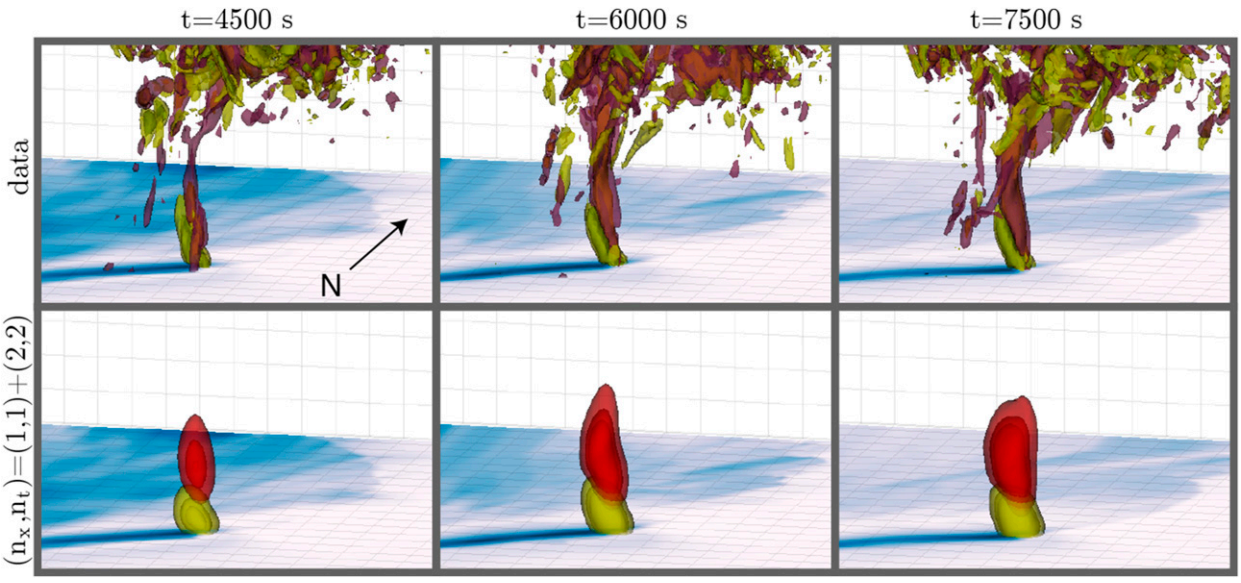

FIG. 3. As in Fig. 2, but analyzing vertical vorticity stretching. Yellowish green indicates positive stretching; red indicates negative stretching. (top) For the data, the contours were $\sigma = \{-1, -0.6, -0.3, 0.3, 0.6, 1\} \times 10^{-3}\ s^{-2}$. (bottom) For the σ_{EFD} estimates, five equally spaced contours in the range $\{0.02, 0.1\} \times 10^{-3}\ s^{-2}$ were used for $\sigma_{EFD}(1, 1)$, which is the positive stretching mode (yellowish green), and five equally spaced contours in the range $\{-0.1, -0.02\} \times 10^{-3}\ s^{-2}$ were used or $\sigma_{EFD}(2, 2)$, which is the negative stretching mode (red). Mode surfaces are colored by mode values on the surface scaled by the mode eigenvalue and therefore in σ units. View is toward the north.

capture the vigorous (positive) stretching associated with the TLV, whereas EFD modes $\sigma_{EFD}(2, 2)$ capture the elevated region of negative stretching. In this case, the second EFD mode is not associated with tornadogenesis or tornado maintenance but, rather, identifies a persistent region within the updraft where the stretching term is consistently negative.

In Fig. 4, we explore vorticity magnitude. Contoured model data reveal large local values of vorticity magnitude throughout the depth of the TLV as would be expected but, also, an enhanced region of vorticity magnitude along and behind the storm's FFDB, roughly consistent with the location of the streamwise vorticity current in Orf et al. (2017). In this case, both EFD analysis modes tell a similar story, keying in on both the vorticity found in the TLV as well as the region of vorticity along the FFDB. The EFD modes, however, do not focus on the more transient and less organized vorticity regions aloft, including some with similar magnitudes of vorticity.

In Fig. 5, we focus on the vorticity magnitude tracts in ER500 at three different model times and the tracts generated from $\omega_{EFD}(1, 1)$ analysis at these times. While interpretation of these tracts is difficult owing to the sheer number of pathways found, some general statements can be made. In all three EFD analyses, a bundle of tracts is found throughout the depth of the mesocyclone with a large concentration of tracts connected to the bottom and top of this bundle, primarily in the direction of the storm's forward flank. The top view reveals a consistent broad swath of tracts primarily spanning the storm's forward flank, with more variability in tracts density in the rear flank. The view looking southwest reveals a bundle of tracts along and slightly behind the FFDB, collocated with the region of enhanced (horizontal) vorticity indicated in Fig. 4 that is located where the SVC is found in Orf et al. (2017). Regions of increased tract density correspond to particularly spatially and temporally coherent vorticity structures and thus would be expected to be of importance in the development and maintenance of features such as tornado-like vortices. The validity of this hypothesis will be explored in future work.

In Fig. 6, vorticity magnitude and EFD analysis of vorticity magnitude at $t = 6000$ s is displayed, focusing on the region of the simulated storm's low-level mesocyclone. The top panel contains two semitransparent contours of vorticity magnitude showing the erect portion of rotation directly above the location of strongest surface horizontal winds associated with the TLV. The small extension of (primarily horizontal) vorticity along the forward flank of the storm is also apparent and is roughly collocated where the SVC was found in Orf et al. (2017). An $\omega_{EFD}(1, 1)$ analysis of vorticity captures these features, and the tract's figure reveals a set of pathways along and slightly behind the FFDB, in

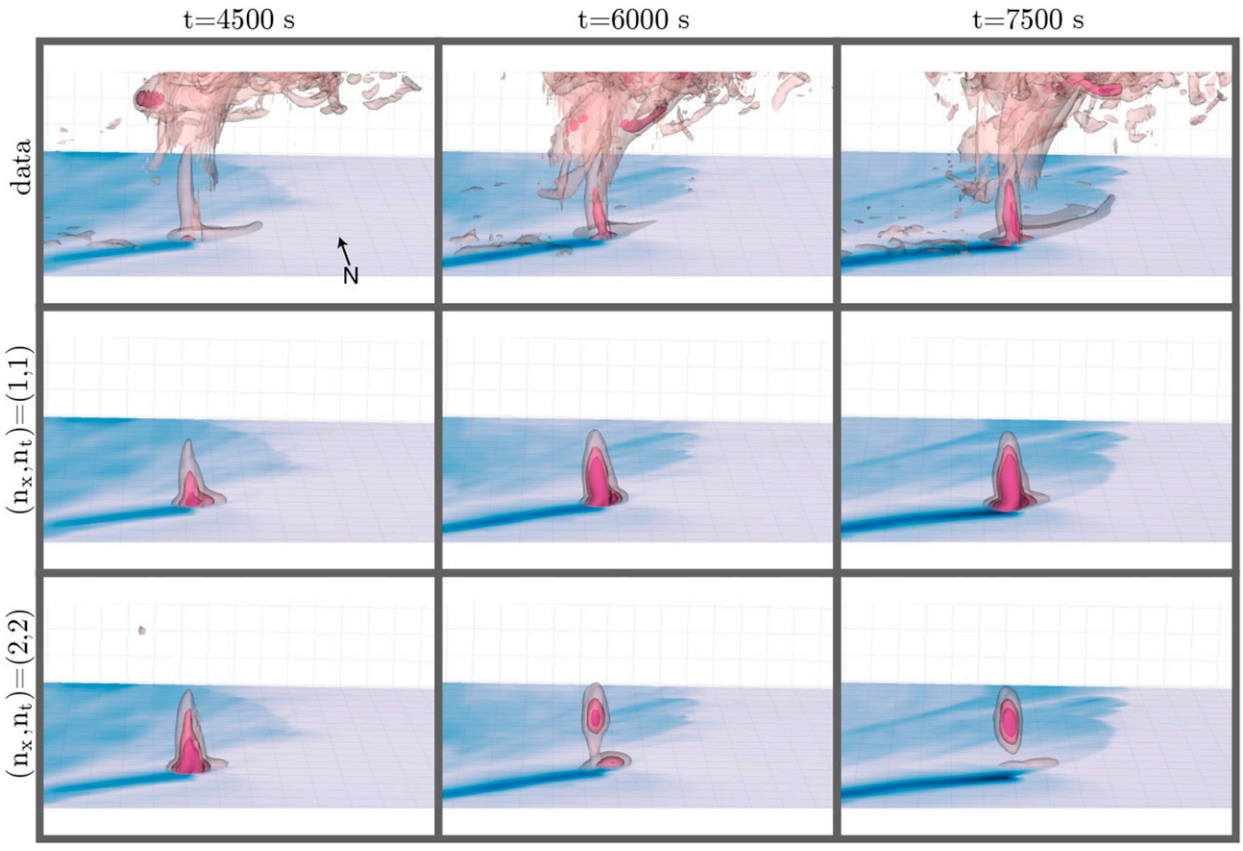

FIG. 4. As in Fig. 2, but analyzing vorticity magnitude $|\boldsymbol{\omega}|$. Five contours equally spaced in the range $\{0, 0.15\}$ s^{-1} were plotted for the data. The ω_{EFD} modes are scaled by the mode eigenvalue and therefore in vorticity units. Five contours in the range $\{0, 0.15\}$ s^{-1} are shown. View is toward the north. Surface shading is as in ω units.

addition to denser regions of elevated tracts that extend into the environment primarily to the east of the storm.

It should be reinforced that this analysis of ER500 is cursory and our main goal here is to validate the EFD approach on a modeled storm in a previously studied environment that contains a persistent vigorous mesocyclone/TLV. ER500 resolution is insufficient to capture many if not most of the features described in Orf et al. (2017) and the fact that EFD analysis is capturing apparently salient features at this resolution is encouraging and will set the stage for future analysis of data at much higher spatial and temporal resolution.

The different spatial and temporal scales reveal different spatial–temporal patterns of the evolving vorticity field and the associated vorticity tracts. These results are achieved by extending the coupling length in space and time, respectively, to higher orders. In practice, our implementation allows an arbitrary number of spatial coupling levels n_s and temporal coupling levels n_t and all combinations of the two in order to produce an $n_s \times n_t$ matrix of resultant EFD time series at different spatial and temporal mixtures of scales. For purpose of the current paper, we have only the diagonal elements of this matrix, where both spatial and temporal correlations lengths are incremented in step.

6. Application to DOW mobile Doppler radar data

a. Data collection and preprocessing

Data analyzed in this study were obtained by DOW (Wurman et al. 1997) MDRs during VORTEX2 (Wurman et al. 2012; Kosiba et al. 2013) in a storm producing a tornado in Goshen County, Wyoming, on 5 June 2009. DOW6 and DOW7 collected synchronized volumes comprising 12 elevation angles (0.5°–16°) every 2 min. Edited radar data (ground clutter was removed and aliased velocities were dealiased) were objectively analyzed to a 40 km × 40 km × 10 km Cartesian grid having a 0.25-km grid spacing using the two-pass Barnes successive corrections method (Majcen et al. 2008). The amount of smoothing was determined by a conservative estimate of the data spacing d in the region of the storm that was scanned [see Markowski et al. (2012a) for more

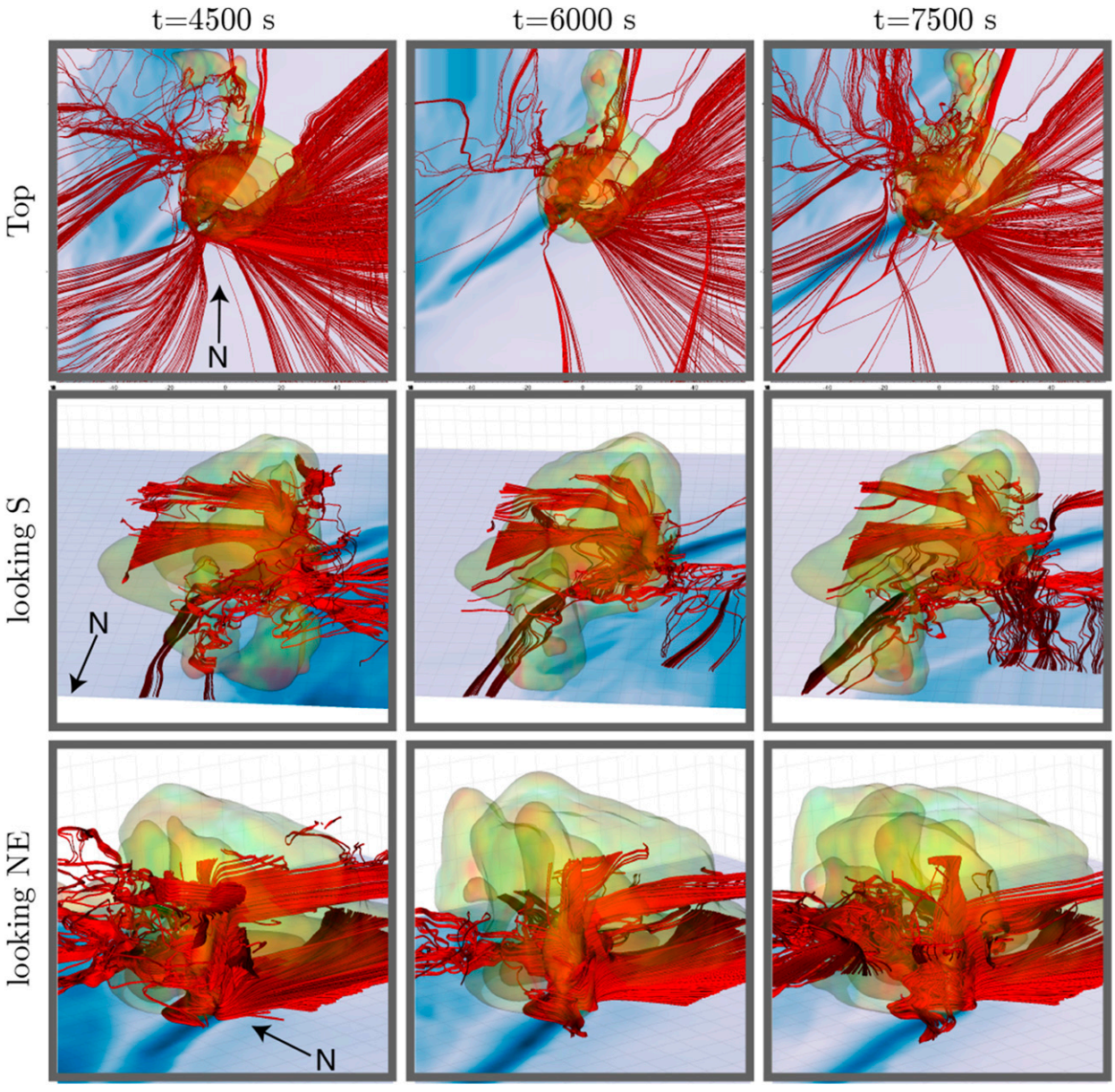

FIG. 5. ER500 EFD analysis showing vorticity tracts (red tubes) and reflectivity EFD isosurfaces (displayed as in Fig. 2) at three different times—(left to right) 4500, 6000, and 7500 s—from three different views: (top) from the top down, (middle) looking south, and (bottom) looking northeast. Surface shading is as in Fig. 2.

details]. Data fields of radar reflectivity and Doppler velocity were interpolated onto 17 three-dimensional Cartesian grids covering 12-min periods from 2142 to 2214 UTC, and dual-Doppler techniques were employed to calculate the orthogonal components of the wind (north–south, east–west, and upward–downward), as described in Kosiba et al. (2013).

b. *EFD analysis*

Figure 7 and Fig. 8 contain contours of objectively analyzed DOW data from the Goshen supercell at 2148, 2156, and 2204 UTC (top row) as well as multiple EFD analyses modes. These times cover the period where rapid intensification of low-level rotation and tornadogenesis was observed (Markowski et al. 2012b; Kosiba et al. 2013). A cursory analysis of EFD data suggests that mode $dBZ_{EFD}(1, 1)$ most faithfully captures the previously documented salient reflectivity characteristics of the observed storm, indicating a clearly defined weak-echo region and hook echo with associated reflectivity maxima extending throughout the depth of the observed storm and a broad region of reflectivity with associated

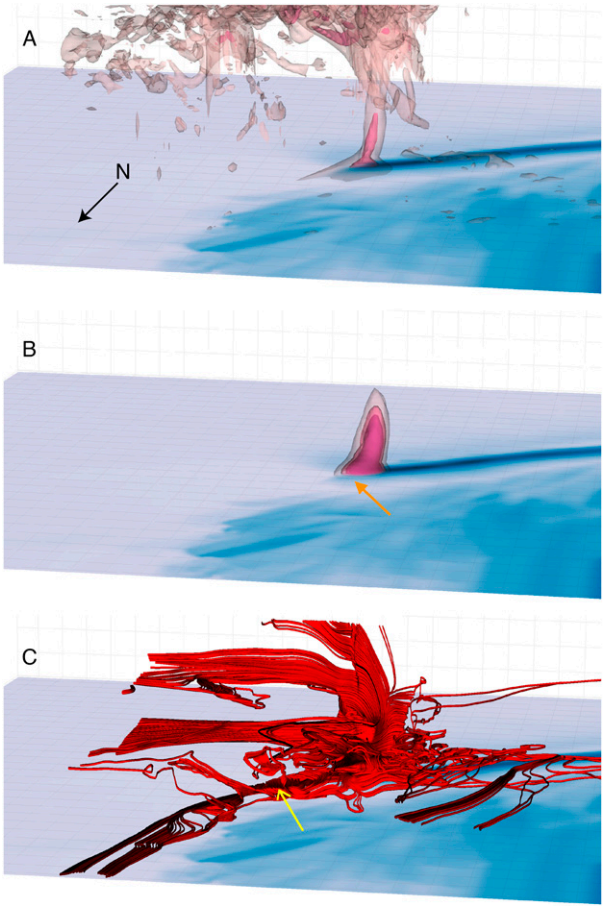

FIG. 6. ER500 simulation data analysis. (a) A single time frame from Fig. 4 of the vorticity magnitude $|\boldsymbol{\omega}|$ in the data to (b) the first EFD mode estimated $|\boldsymbol{\omega}|_{\mathrm{EFD}}$, where the orange arrow points to the "foot" in the local vorticity profile, and (c) the vorticity tracts generated from the first EFD vorticity mode, where the yellow arrow indicates the location of a feature in the model data that suggests a marginally resolved streamwise vorticity current, which overlaps with a bundle of tracts that follow along and behind the storm's forward-flank downdraft boundary. The view is from the north looking along the leading edge of the storm. Surface shading is as in Fig. 4.

maxima throughout the storm's forward flank, as well as a low-reflectivity ribbon (LRR) (Wurman et al. 2012). The quantity $\mathrm{dBZ}_{\mathrm{EFD}}(2, 2)$ analysis presents a notably different reflectivity pattern more representative of the outer portion of the tip of the hook echo, extrusions to the east and north, and a relative minimum extending northeastward of the hook. The quantity $\mathrm{dBZ}_{\mathrm{EFD}}(3, 3)$ presents an even more prominent larger-scale local circulation about the edge of the hook tip that appears highly spatially correlated with the leading and rear edges of the storm. From the perspective of EFD, these results represent larger spatial and temporal variations, such as the circulation around the edge of the hook tip that then extend from the hook tip out to the rear and forward flanks of the storm. Generally, these differences between the modes demonstrate that reflectivity patterns along the edges of the supercell are more consistent across longer distances and times, while the storms' cores (updraft and points downshear) exhibit a higher degree of short-wave, short-duration spatiotemporal variability. We speculate that this is due to short-duration physical processes such as updraft pulsing and hail fallout events. Understanding the precise physical mechanisms underlaying EFD-detected features will require more in-depth analysis of observational and simulation data.

Figures 9 and 10 include contours of vertical vorticity stretching (σ) and vertical vorticity (ζ) at the same times as shown in the previous figures. As this period of the storm covered intensification of low-level rotation, tornadogenesis, and tornado intensification, one would expect to see enhanced σ followed by rapidly growing ζ. EFD analysis of these fields captures these processes, with σ_{EFD} contours prominent at 2156 and 2204 UTC, corresponding to a column of σ shown in the DOW data contours. As in the simulation data, the dipole structure of negative and positive stretching are clearly evident in the estimated EFD modes. The ζ fields show a similar pattern with somewhat disorganized rotation indicated at 2148 UTC, leading to a vertical column of contours at 2156 UTC and an erect, strong region of ζ_{EFD} at 2204 UTC, also clearly present in the DOW ζ contours. EFD analysis automatically captures salient processes of interest to tornadogenesis while ignoring much of the remaining noisy data shown many kilometers away from the tornado as evidenced by comparing the top rows of Figs. 9 and 10 to the EFD contours below.

In Fig. 11, ζ tracts are calculated for three time frames of DOW data and shown from three different views. One must be careful when comparing vertical vorticity DOW tracts to the total vorticity ER500 tracts in Fig. 5. In addition, unlike the simulation data, the DOW data are incomplete or nonexistent near the ground (the lowest scan height is ≈200–300 m) so vorticity tracts running parallel to the surface at low levels will not be detected. EFD analyses over time reveal a dense column of vertically oriented tracts that extend from the ground upward, roughly collocated with the reflectivity maximum at the tip of the hook echo, adjacent to the developing tornado, as well as additional tract clusters extending into the rear and forward flanks of the storm. Note that at $t = 2158$ UTC (and other frames not shown) there are apparently near-ground looping vortex tracts, consistent with the "vortex arches" that have been detected by traditional means (e.g., Markowski et al. 2012a; Kosiba et al. 2013).

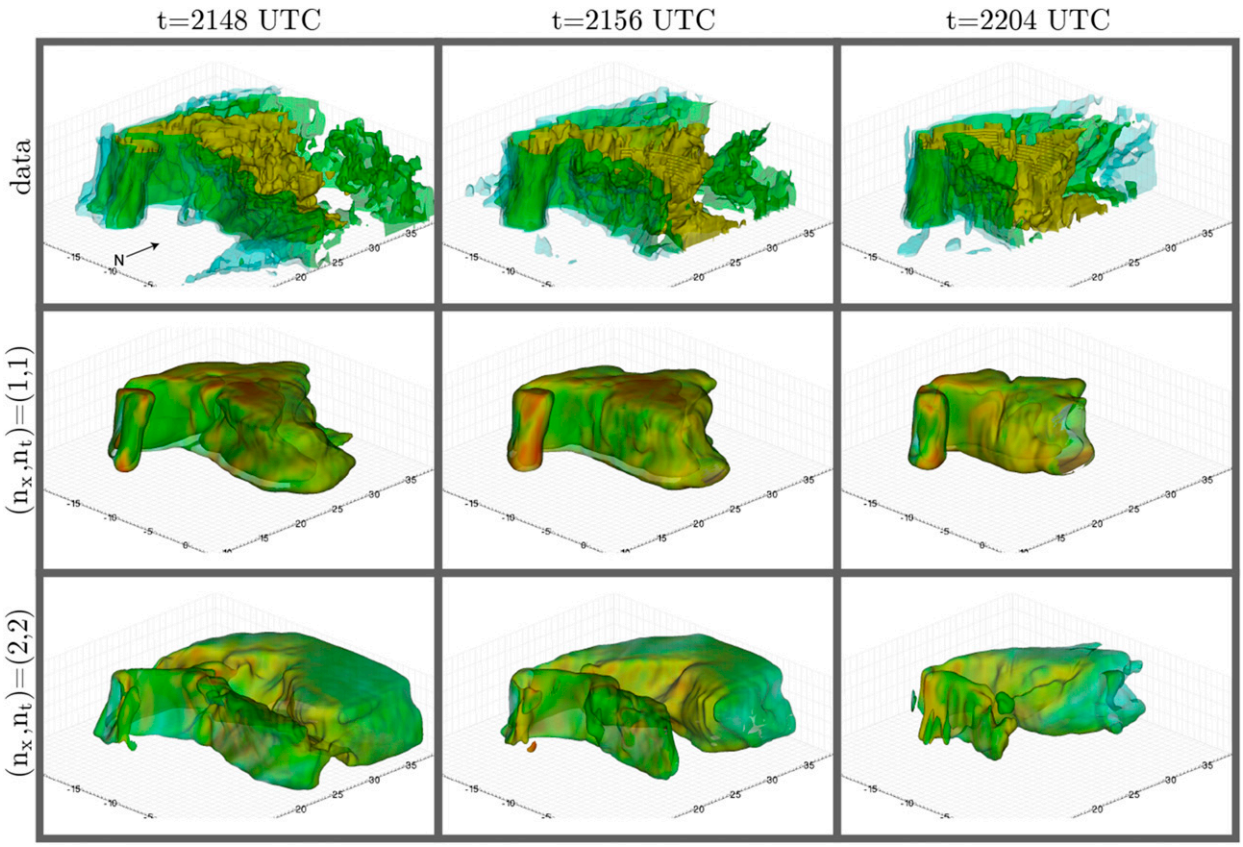

FIG. 7. DOW data analysis. A comparison of dBZ contours (top) in the data at three times—(left to right) 2148, 2156, and 2204 UTC—with (middle),(bottom) the two estimated EFD dBZ_{EFD} modes: $(n_x, n_t) = (1, 1)$ and $(n_x, n_t) = (2, 2)$ at the same times. Six equally spaced contours in the range {0, 66} dBZ were plotted for the data. For the dBZ_{EFD} modes, five equally spaced contours from 0 to the mode maximum value are shown. The coloring is the data dBZ on the contour surface locations.

All of the parameter estimate volumes can be combined, of course, which is essential for understanding the complete dynamics of the evolving fields. For example, a localized and coherent feature of interest identified and previously documented in the dBZ field in these data as the DRC (Markowski et al. 2012b; Kosiba et al. 2013) is evident in dB$Z_{\mathrm{EFD}}(1, 1)$, as seen in the highlighted view of Fig. 7 shown in Fig. 12 where it is combined with the first EFD mode for vertical vorticity $\zeta_{\mathrm{EFD}}(1, 1)$.

Overall, these figures demonstrate that spatially and temporally coherent patterns are revealed objectively using EFD, as opposed to being revealed subjectively through expert analysis and evaluation as is now standard. The ability of EFD to automatically detect spatially and temporally coherent features in the data provides a unique capability that can augment traditional multiple-Doppler techniques.

Current analysis approaches, such as in Kosiba et al. (2013), typically involve the subjective editing of these contour lines, which is not only time consuming, but necessarily dependent upon the skill (and biases) of the individual doing the analysis. The EFD method provides an automated, objective approach for detecting complex spatiotemporal features of the storm structure. While diagnosing and evaluating how these detected phenomena are associated with tornadogenesis using EFD is a topic for future work, it is clear that EFD offers the potential for enhancing these types of analysis.

The ability of EFD to detect features at different spatial and temporal scales, such as is evident in the estimated fields dBZ_{EFD}, σ_{EFD}, and ζ_{EFD}, and the associated vorticity lines, is an important feature that we anticipate will provide insight into storm structure and evolution in future work on these scale-dependent parameter estimates.

7. Discussion and conclusions

Many physical systems exhibit highly nonlinear and non-Gaussian characteristics, and this is certainly true of severe storms (e.g., Bluestein 2007). As detection systems such as MDR attain finer spatial and temporal

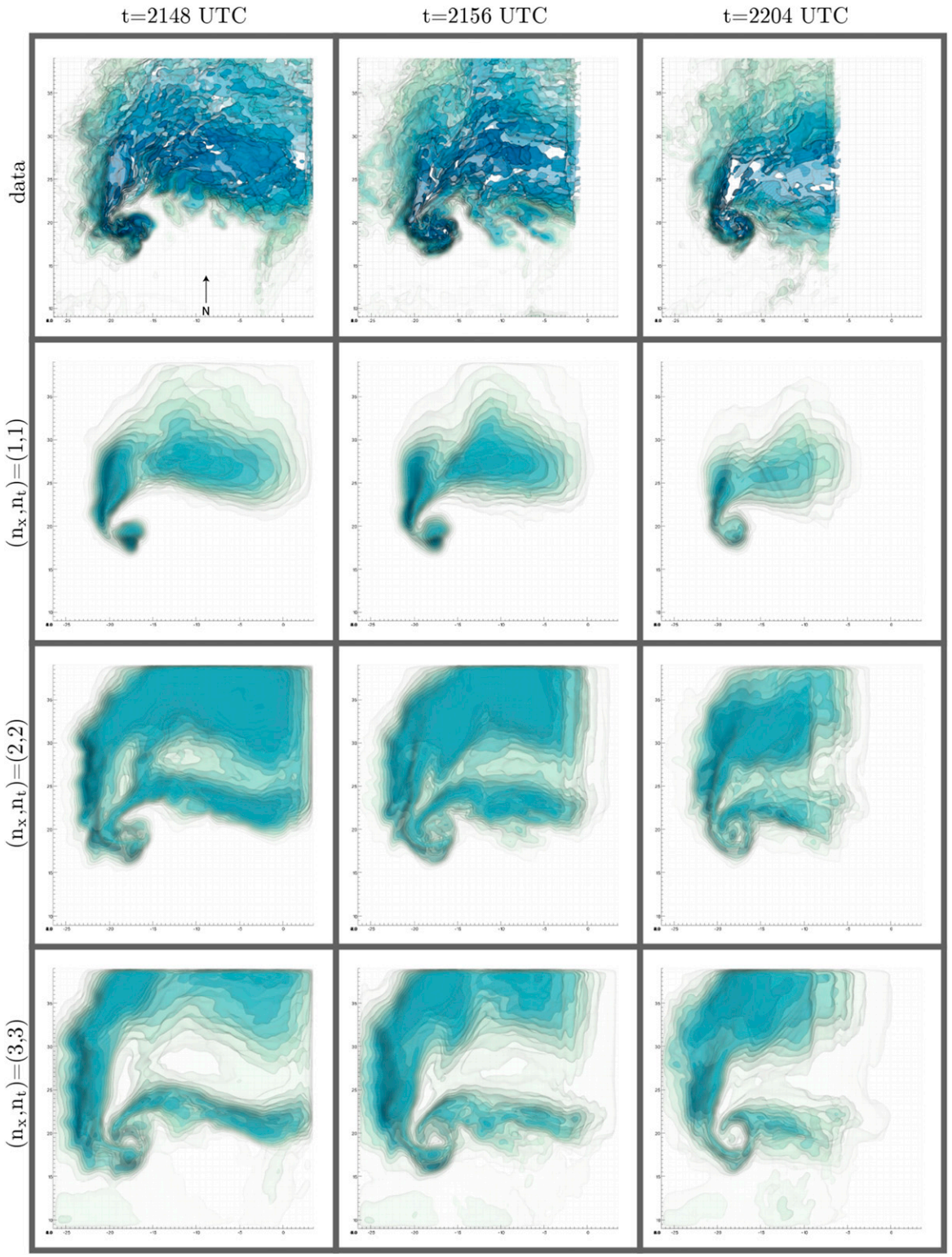

FIG. 8. DOW data analysis. A comparison of dBZ contours (top) in the data at three times—(left to right) 2148, 2156, and 2204 UTC—with (bottom three rows) the estimated EFD dBZ_{EFD} modes at three different spatial–temporal scales: nearest neighbor $(n_x, n_t) = (1, 1)$, fourth-order neighbor $(n_x, n_t) = (2, 2)$, and eighth-order neighbor $(n_x, n_t) = (3, 3)$. The view is from the top from which the characteristic "hook" is visible. The bottom of the each plot is south and the top is north. Ten contours equally spaced in the range {0, 66} dBZ were plotted for the data. For the EFD modes, 10 equally spaced contours are plotted from 0 to the mode maximum. Coloring is by mode value on the surface.

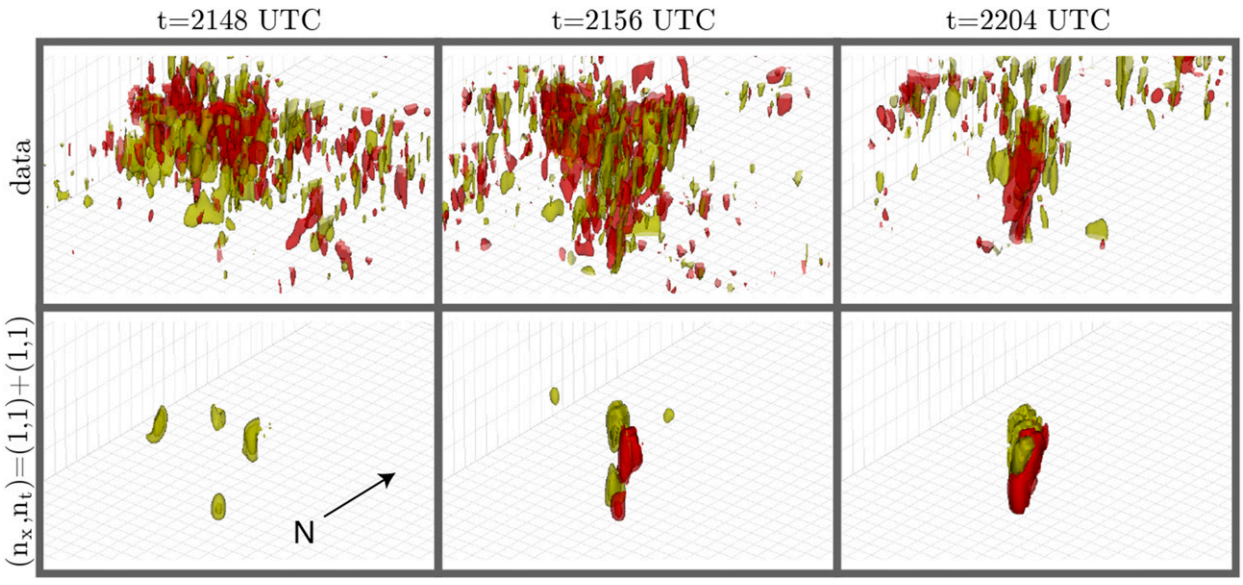

FIG. 9. DOW data analysis. A comparison of σ contours (top) in the data at three different times—(left to right) 2148, 2156, and 2204 UTC—with (bottom) two estimated EFD σ_{EFD} modes: $(n_x, n_t) = (1, 1)$ computed separately for both positive and negative stretching in the data. For the data, contours were $\sigma = \{-65, -45, -25, -5, 5, 25, 45, 65\} \times 10^{-4}\,\mathrm{s}^{-2}$. The σ_{EFD} modes are scaled by the mode eigenvalue and therefore are in σ units. For both positive (yellowish green) and negative (red) stretching modes $\sigma_{\mathrm{EFD}}(1, 1)$ five equally log-spaced contours in the range {0.01, 3} were used.

resolution, these features become more evident in the data. It is often not appreciated that simple contouring of parametric surfaces is implicitly a linear estimation method. While the underlying surface may have been generated by highly nonlinear processes, the process of contouring implicitly assumes a linear relationship between the contour value(s) and the associated parameter surface. Accurately estimating parameters from such systems therefore requires analysis methods capable of incorporating nonlinear and non-Gaussian behavior. Unfortunately, in many areas of scientific research where quantitative measures of dynamical processes are of interest the use of ''traditional'' analysis methods that are predicated on linear and Gaussian models can be insufficient for more complex systems. This is the case, for example, with principal components analysis (PCA), often called empirical orthogonal functions (EOF) in meteorological applications (Lorenz 1956; Obukhov 1947, 1960; Craddock 1973), which relies on the first and second moments of the data to minimize the covariance of the estimates, thereby implicitly assuming Gaussianity of the data, in addition to linearity. Methods have been developed to attempt to analyze nonlinear and non-Gaussian systems, the most popular being independent components analysis (ICA) (Bell and Sejnowski 1995; Comon 1994; McKeown et al. 1998; Beckmann and Smith 2004). However, this procedure is, in our view, rather ad hoc, as we have detailed elsewhere (Frank and Galinsky 2016b). Our approach, the entropy field decomposition (EFD) (Frank and Galinsky 2016a,b), is developed directly from within the logical framework of probability theory which has no implicit constraints on anything other than logical consistency. Expressing the general statement of Bayes's theorem [Eq. (1a)] in the language of field theory [Eq. (3a)] facilitates the construction of probabilities in terms of nonlinear and non-Gaussian components, at the expense of a very large parameter space. But the inclusion of prior information (via the prior probability density in Bayes's theorem) of the coupling structure within the data itself helps solve this dimensionality problem by the theory of entropy spectrum pathways (ESP) (Frank and Galinsky 2014), which extracts only the most relevant parameter configurations thereby reducing the computational problem to dimensions easily determined numerically.

In the context of DOW and other MDR data, EFD analysis provides a new formalism for the estimation of nonlinear spatiotemporal coherences in the data not attainable from simply contouring of parameter surfaces. The formalism is based on a Bayesian framework and thus is conservative in the sense that it derives estimates based on required consistency with prior information within the data. Thus, while contouring remains a valuable technique for depicting the evolution of parametric fields, it is not a rigorous formalism for

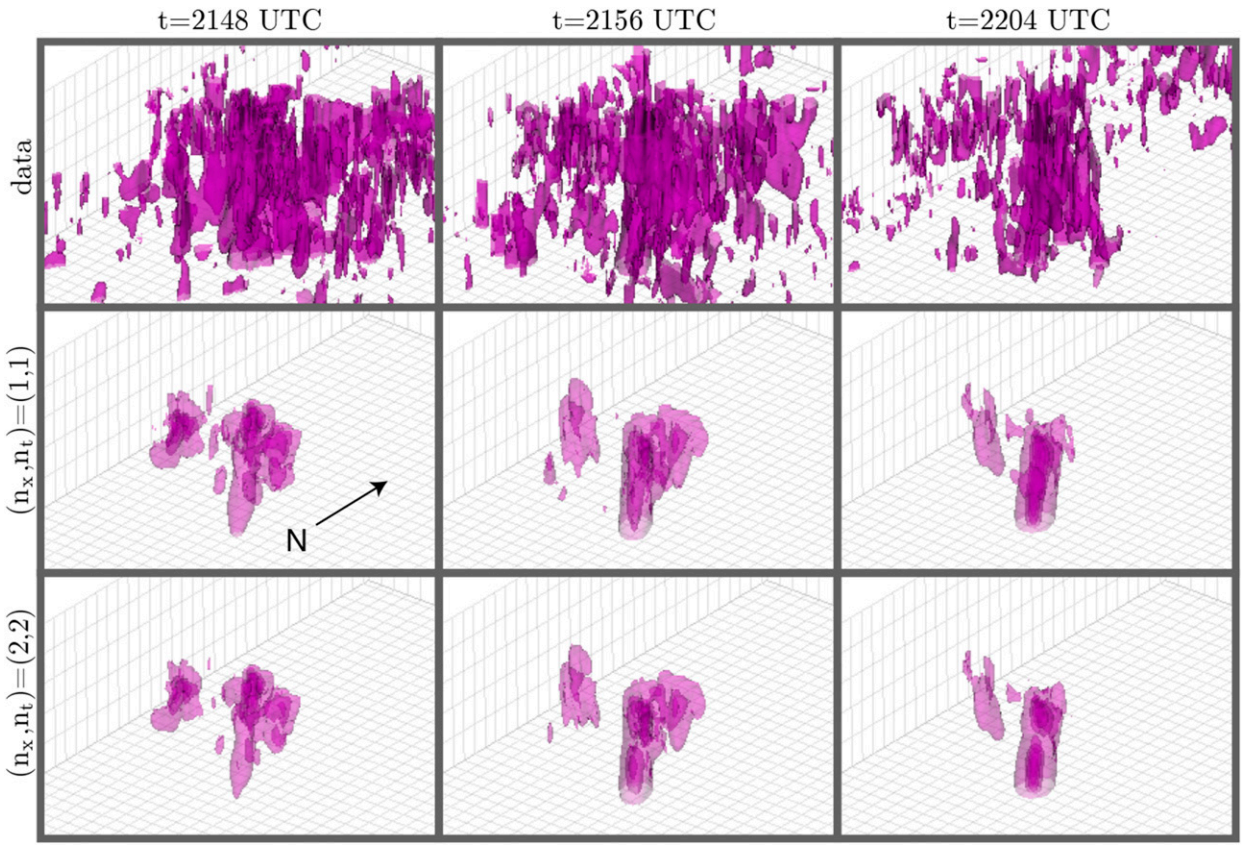

FIG. 10. DOW data analysis. A comparison of vertical vorticity contours (top) in the data at three different times—(left to right) 2148, 2156, and 2204 UTC—with (middle),(bottom) two estimated ζ_{EFD} modes: $(n_x, n_t) = (1, 1)$ and $(n_x, n_t) = (2, 2)$ at the same time points. View is looking toward the northwest. Five contours equally spaced in the range $\zeta = \{0, 0.045\}$ s^{-1} were plotted for the data. The ζ_{EFD} modes are scaled by the mode eigenvalue and therefore in ζ units. Six equally spaced contours in the range $|\boldsymbol{\omega}| = \{0, 0.045\}$ s^{-1} values are shown.

detecting coherent nonlinear and non-Gaussian processes. This capability of EFD thus provides unique capabilities that can augment traditional contour analysis.

We present an example of where EFD analysis resolves an evolving feature in the velocity field, stretching of vertical vorticity, perhaps better and/or earlier than traditional dual-Doppler analysis. The approach allows us to define coupling in terms of parameters resulting from the standard objective analysis, giving a flexibility to use scalar or vector (or even multiscale tensor) coupling. Using the general analysis outlined in Frank and Galinsky (2016b,a), this produces ranked modes of the storm that reveal clearly the spatiotemporal modes of the critical variables in tornadogenesis such as vertical vorticity stretching and vertical vorticity. The generation and intensification of low-level rotation is clearly indicated in the major modes detected by EFD and appears to be consistent with recent theories focusing on the role of the descending reflectivity core (Markowski et al. 2012a,b; Kosiba et al. 2013). This core, and the convergence, intensification, and coalescence of the vertical vorticity as mediated by the vertical vorticity stretching, are automatically detected and quantified by our method, illustrating how the technique can provide new insight into the quantitative dynamics of tornadogenesis.

Overall the EFD approach combines both local and multiscale nonlocal properties of the underlying field in a rigorous way. These properties can include boundary conditions, conditions on internal interfaces (if any), short- and long-range spatial and temporal correlations between various scalar, and vector or tensorial parameters. This unique ability of EFD to detect patterns in highly multivariate data through simultaneous processing of many pieces of information allows detection of subtle features or localizations that would otherwise be missed by the conventional analyses that assume linearity and Gaussianity.

One of the interesting, but also perhaps the most confusing, aspects of the EFD method is its ability to create modes with sensitivity to multiple spatial and temporal scales. This results in multiple modes that uncover complex and subtle spatiotemporal patterns not

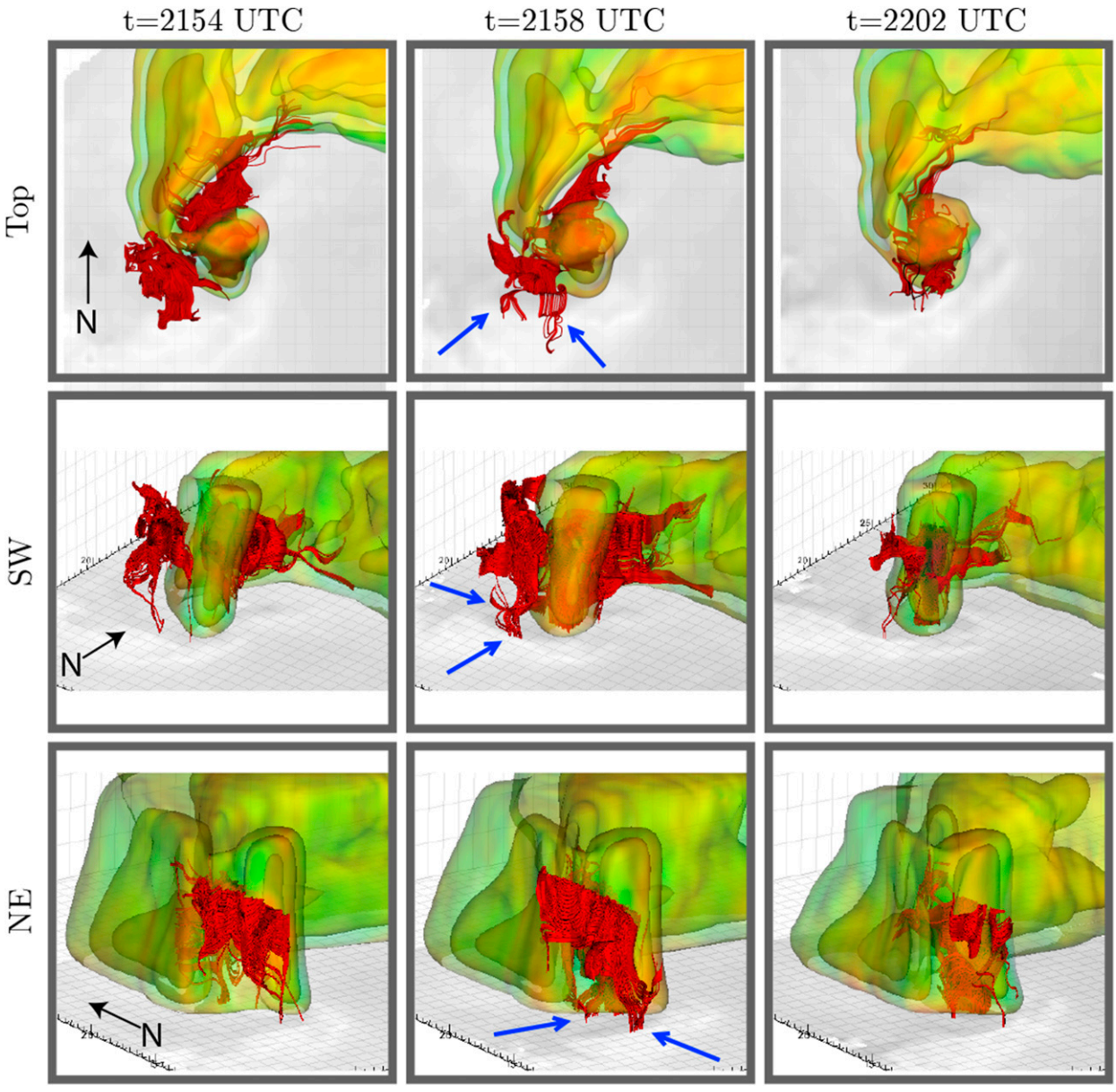

FIG. 11. DOW EFD analysis showing vorticity tracts (red tubes) and reflectivity EFD isosurfaces (displayed as in Fig. 2) at three different times—(left to right) 2148, 2156, and 2204 UTC—from three different views: (top) from the top down, (middle) looking northwest, and (bottom) looking northeast. Arrows at t = 2158 UTC indicate vortex arches.

always detected by traditional means. The result can be patterns that are unfamiliar from analysis results using traditional methods. This is most certainly the case in the EFD dBZ modes detected in the DOW data (Fig. 8), where the dB$Z_{\mathrm{EFD}}(1, 1)$ mode represents the typical hook-echo structure but the higher-order modes [dB$Z_{\mathrm{EFD}}(2, 2)$ and dB$Z_{\mathrm{EFD}}(3, 3)$] show highly coherent features different from dB$Z_{\mathrm{EFD}}(1, 1)$ (as they should) related to larger-scale spatiotemporal processes and thus do not have the same appearance as the standard hook-echo reflectivity structure. It is worth noting that a similar situation exists in the application of the EFD to brain imaging data (Frank and Galinsky 2016b), where it uncovered patterns of brain activity not observed with traditional techniques incapable of detecting more subtle nonlinear phenomena. These spatiotemporal patterns do exist in the data because we know EFD works, but what these new patterns ''mean'' is a question for neuroscientists. Similarly, we can attest to the robust nature of EFD method to the meteorological data analyzed in this paper, but the ''meaning'' of the findings is necessarily the subject of future work.

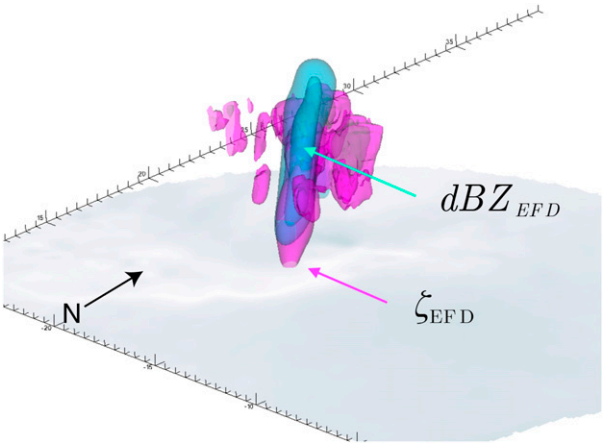

FIG. 12. DOW data analysis. Highlighted view of Fig. 7 showing three $dBZ_{EFD}(1, 1)$ contours from 0.5 max$[dBZ_{EFD}(1, 1)]$ to max $[dBZ_{EFD}(1, 1)]$ in cyan at t = 2148 UTC along with $\zeta_{EFD}(1, 1)$ contours in magenta from Fig. 10. For clarity, only parameter estimates within a box bounded by $\{x_{min}, x_{max}, y_{min}, y_{max}, z_{min}, z_{max}\}$ = $\{-20, -15, 16, 22, 0, 4\}$ km are shown. The dBZ_{EFD} contours are consistent with the DRC described in Markowski et al. (2012b, their Fig. 20d). The view is looking northwest.

The EFD estimation of the modes of vertical vorticity stretching σ (Fig. 3 and Fig. 9) presents an interesting example. Though fully aware that positive stretching (σ^+) is generally of most interest in the study of tornadogenesis, as it is a critical dynamical feature that enhances vertical vorticity, we chose to also display the negative stretching (σ^-) because it is a related dynamical feature that EFD detects since it appears as a strong couplet with σ^+ near the TLV. This is a clear demonstration that EFD can estimate distinct complex dynamical spatiotemporal features.

The EFD estimation of σ also brings to the forefront an important general issue in MDR analysis. In the simulation results there is high spatial and temporal resolution data with effectively infinite SNR and no missing data points. In this case, the EFD analysis resulted in a clear separation of σ^+ in mode $\sigma_{EFD}(1, 1)$ and σ^- in mode $\sigma_{EFD}(2, 2)$ (Fig. 3). But DOW MDR data are, of course, subject to numerous observational realities that can result in noisy or missing data and require significant preprocessing before it can be subject to analysis (see, e.g., Wurman et al. 2007a). The EFD algorithm implemented in this paper is careful about identifying bad or missing data points and thus makes the best estimates of the modes even in the presence of realistic imperfections in the data. Moreover, the computation of the σ field from the raw data requires not only estimation of the vertical wind profile but the notoriously noise-sensitive calculation of derivatives (e.g., Wurman et al. 2007a). The resulting σ field in the data was quite noisy and so we choose to estimate σ^+_{EFD} from only the positive stretch component of the data (σ^+) and σ^-_{EFD} from only the negative stretch component of the data (σ^-). Nevertheless, EFD was able to clearly distinguish the σ couplet, though in this case each appeared as the first EFD mode [i.e., $\sigma^+_{EFD}(1, 1)$ and σ^-_{EFD} $(1, 1)$] in the separate analyses.

There is perhaps an important lesson in this example that has a precedent in the analysis of FMRI data, for which the EFD analysis was initially developed. Initially the focus in FMRI was on general linear models that assumed Gaussian noise (Poline and Brett 2012). However, it was in part the failure (or, at least, the nonoptimality) of this approach that led to the recognition that the most important noise sources were non-Gaussian, being physiological in nature (e.g., Frank et al. 2001), and thus required a more general formalism (e.g., Frank et al. 1998) that could ultimately be used to incorporate more complex realistic noise sources (e.g., Woolrich et al. 2004). The lesson is that having a logically consistent formalism for the analysis of complex nonlinear processes is critical not only in detecting what one expects but also what may not be expected. Simple contouring of derived quantities will not provide this type of information. The EFD formalism does not require any assumptions about the structure of the dynamical processes or the noise and can incorporate models of either. This suggests that a potentially fruitful area of future work will be to integrate the estimation of the wind fields themselves directly into the EFD estimation scheme, thereby taking into account all that is known about the radar systems, the ground clutter, etc., that contribute to inaccuracies in the estimates of the quantities of interest, such as σ.

While the EFD method presented in this paper has a broad range of application, our particular interest is in the development and maintenance of tornadoes, particularly those that are long track and violent. Understanding the mechanisms of tornado formation has long been a focus of severe weather research (e.g., Davies-Jones et al. 2001; Beck et al. 2006; Markowski and Richardson 2009; Markowski et al. 2012a,b; Marquis et al. 2008, 2012; Wurman and Kosiba 2013; Kosiba et al. 2013; Marquis et al. 2014). In addition to its basic scientific importance, the obvious major benefit of the capability of deriving tornadic signatures objectively and automatically in real data is the possibility that they may be used to forecast events in near–real time and be used to enhance public warning systems. However, the complexity of the evolution of the wind and precipitation fields in pretornadic and tornadic storms currently precludes a satisfactory analytical approach and, while numerical simulations are promising (e.g., Wicker and

Wilhelmson 1995; Markowski et al. 2003; Markowski and Richardson 2014; Orf et al. 2017), currently they remain limited in their ability to simulate tornadic events. The analysis of observational data therefore remains a primary source of information regarding tornadogenesis. Traditional multiple-Doppler analyses of severe storms (e.g., Kosiba et al. 2013; Markowski et al. 2012a) necessarily employ expert analysis of subjectively detected/identified features, contour intervals, and choices of vortex lines and trajectories owing to the complexity of the evolving vorticity fields.

One approach is to calculate backward trajectories by choosing a region of interest and integrating backward in time to determine where the parcels of air in this region originated. However, this approach has been shown to be susceptible to significant numerical errors (Dahl et al. 2012). Alternatively, forward integration whereby wind fields are integrated forward in time then choosing the parcels that pass through the region of interest is much more stable (Coffer and Parker 2017). Comparison of traditional Lagrangian vorticity budget analysis with our trajectory method remains an interesting question for future work. In particular, what is the relationship between vorticity tracts and regions where generated vorticity is tilted and stretched to produce tornadoes?

There are other potential uses for the EFD algorithm. Analysis of velocity observations from a single Doppler radar presents a significant challenge. Although beyond the scope of the present study, the robustness of EFD for single-Doppler analysis of mesocyclones and tornadoes could potentially be tested through data denial experiments. This would allow a test of the robustness of the EFD estimation with single-radar data by comparing, for example, the estimated vorticity fields and tracts generated with a single radar and with both radars. While the current paper focuses on MDR data in severe local storms, the EFD algorithm is appropriate for radar data collected at much larger scale and would be useful for the detection of modes in mesoscale radar data, such as from the NEXRAD WSR-88D system.

While MDR such as those used in this study have the advantage over operational radar systems because of their low-level sampling and higher spatial resolution, this comes at the cost of a significant amount of necessary preprocessing including noise removal, synchronization of the dual-Doppler measurements, and other editing and censoring of raw data. However, the EFD approach is very general and can be used with a wide variety of data. Of particular relevance to operational radar systems would be the analysis of single-Doppler measurements and the estimates of ΔV or azimuthal shear, for example.

There are certainly a much broader range of parameters that are influential in tornadogenesis than have been discussed in the present paper that will ultimately need to be included in future analysis in order to develop a more complete picture of the dynamics of tornadogenesis and the maintenance of strong, long-lived tornadoes. From a long-term perspective, it is our belief that the application of EFD to severe weather prediction using radar data offers the possibility of an analysis system capable of being used in conjunction with operational weather radar instrumentation to develop more automated early-warning systems. Since these techniques are automated, not requiring time-intensive scientific analysis, these may provide a path toward more timely tornado and other severe weather warnings.

We also note that the current paper computes the EFD modes from complete (in time) datasets. However, the theoretical formulation of EFD (Frank and Galinsky 2016a,b) is Bayesian and easily facilitates the prediction of the current ''state'' of a physical system as more information is gathered. Thus it is natural to consider its application to problems of data assimilation (e.g., Snyder and Zhang 2003; Marquis et al. 2014), which are ubiquitous in a multitude of meteorological problems, and will be considered in future work.

Acknowledgments. LRF and VLG were supported by NSF Grants DBI-1143389, DBI-1147260, EF-0850369, PHY-1201238, and ACI-1550405. LO was supported by the Cooperative Institute for Meteorological Satellite Studies (CIMSS) and NSF Grants ACI-1550405 and ACI-1614973. JMW and DOWs are supported by NSF Grants AGS-1447268, AGS-1361327, and ACI-1550405. Two of us (LRF and JMW) would like to thank the late Herb Stein for his guidance in the field, and for keeping them safe, and LRF would like to thank Dr. Curtis Alexander, Dr. Jeff Beck, and Dr. Jeff Frame for their significant in situ education. We would also like to thank the anonymous reviewers for many helpful suggestions that significantly improved the paper.

APPENDIX

EFD Summary

The data $\{d(x_j, t_i)\}$ are assumed to consist of n measurements in time t_i, $i = 1, \ldots, n$ at N spatial locations x_j, $j = 1, \ldots, N$ [or equivalently $\{d(\xi_l)\}$, where ξ_l, $l = 1, \ldots, nN$ defines a set of space–time locations]. The spatial locations are assumed to be arranged on a Cartesian grid and the sampling times are assumed to be equally

spaced. Neither of these is required in what follows, but merely simplify and clarify the analysis. For most applications in which we are interested, the data d are assumed to be four dimensional, comprising temporal variations in the signal from a volumetric (three spatial dimensions) imaging experiment. Each datum is of the form

$$d(x_j, t_i) = \hat{R}s(x_j, t_i) + e_{i,j}, \tag{A1}$$

where $\hat{R}$ is an operator that represents the response of the measurement system to a signal $s(x_j, t_i)$, and $e_{i,j}$ is the noise with the covariance matrix $\mathbf{\Sigma_e} = \langle \mathbf{ee}^\dagger \rangle$, where † represents the complex conjugate transpose.

The problem can be expressed in the language of IFT [Eq. (3a)] by writing the information Hamiltonian $H(d, s)$ as (Enßlin et al. 2009)

$$H(d,s) = H_0 - j^\dagger s + \frac{1}{2}s^\dagger D^{-1}s + H_i(d,s), \tag{A2}$$

where H_0 is essentially a normalizing constant that can be ignored, D is an information propagator, j is an information source, and † means the complex conjugate transpose. Also H_i is an interaction term (Enßlin et al. 2009)

$$H_i = \sum_{n=1}^{\infty} \frac{1}{n!} \int \cdots \int \Lambda^{(n)}_{s_1 \cdots s_n} s_1 \cdots s_n \, ds_1 \cdots ds_n, \tag{A3}$$

where $\Lambda^{(n)}_{s_1 \cdots s_n}$ terms describe the interaction strength.

When the source term j, the linear information propagator D, and the nonlinear interaction terms $\Lambda^{(n)}_{s_1 \cdots s_n}$ are all known or at least some more or less accurate approximations can be used for their description, the IFT approach provides an effective, powerful, and mathematically elegant way to find an unknown signal s either by using the classical solution at the minimum of Hamiltonian ($\delta H/\delta s = 0$) or with the help of summation methods [e.g., with the help of Feynman diagrams (Feynman 1949; Enßlin et al. 2009)].

But there is a whole class of problems where those terms are unknown and too complex for deriving effective and accurate approximations. In this case the ESP method (Frank and Galinsky 2014), based on the principle of maximum entropy (Jaynes 1957a,b), provides a general and effective way to introduce powerful prior information using coupling between different spatiotemporal points that is available from the data itself. This is accomplished by constructing a so-called coupling matrix that characterizes the relation between locations i and j in the data:

$$Q_{ij} = e^{-\gamma_{ij}}. \tag{A4}$$

Here the γ_{ij} are Lagrange multipliers that describe the relations and depend on some function of the space–time locations i and j. The eigenvalues λ_k and eigenvectors $\boldsymbol{\phi}^{(k)}$ of the coupling matrix $\mathbf{Q}$

$$\sum_j Q_{ij}\phi_j^{(k)} = \lambda_k \phi_i^{(k)} \tag{A5}$$

then formally define the transition probability from location j to location i of the kth mode (or path as it is often called in the random walk theory) as

$$p_{ijk} = \frac{Q_{ji}}{\lambda_k}\frac{\phi_i^{(k)}}{\phi_j^{(k)}}. \tag{A6}$$

For each transition matrix [Eq. (A6)] there is a unique stationary distribution associated with each mode k,

$$\boldsymbol{\mu}^{(k)} = [\boldsymbol{\phi}^{(k)}]^2, \tag{A7}$$

that satisfies

$$\mu_i^{(k)} = \sum_j \mu_j^{(k)} p_{ijk}, \tag{A8}$$

where $\boldsymbol{\mu}^{(1)}$, associated with the largest eigenvalue λ_1, corresponds to the maximum entropy stationary distribution (Burda et al. 2009).

The EFD approach (Frank and Galinsky 2016a,b) adds those coupling matrix priors into the information Hamiltonian [Eq. (A2)] by expanding the signal s into a Fourier expansion using $\{\boldsymbol{\phi}^{(k)}\}$ as the basis functions

$$s_i = \sum_k^K [a_k \phi_i^{(k)} + a_k^\dagger \phi_i^{\dagger,(k)}]. \tag{A9}$$

In this ESP basis the information Hamiltonian [Eq. (A2)] can be written as

$$H(d, a_k) = -j_k^\dagger a_k + \frac{1}{2}a_k^\dagger \mathbf{\Lambda} a_k + \sum_{n=1}^{\infty} \frac{1}{n!} \sum_{k_1}^{K} \cdots \sum_{k_n}^{K} \tilde{\Lambda}^{(n)}_{k_1 \cdots k_n} a_{k_1} \cdots a_{k_n}, \tag{A10}$$

where matrix $\mathbf{\Lambda}$ is the diagonal matrix Diag$\{\lambda_1, \ldots, \lambda_K\}$ composed of the eigenvalues of the coupling matrix, and j_k is the amplitude of kth mode in the expansion of the source j

$$j_k = \int j \boldsymbol{\phi}^{(k)} \, ds \tag{A11}$$

and the new interaction terms $\tilde{\Lambda}^{(n)}$ are

$$\tilde{\Lambda}^{(n)}_{k_1 \cdots k_n} = \int \cdots \int \Lambda^{(n)}_{s_1 \cdots s_n} \phi^{(k_1)} \cdots \phi^{(k_n)} \, ds_1 \cdots ds_n. \tag{A12}$$

For the nonlinear interaction terms $\Lambda^{(n)}_{s_1 \cdots s_n}$ the EFD method again takes coupling into account through factorization of $\Lambda^{(n)}$ in powers of the coupling matrix

$$\Lambda^{(n)}_{s_1\cdots s_n} = \frac{\alpha^{(n)}}{n}\sum_{p=1}^{n}\prod_{\substack{m=1\\m\neq p}}^{n} Q_{pm}, \tag{A13}$$

where $\alpha^{(n)} \lesssim 1/\max(j_k^n/\lambda_k)$, which results in

$$\tilde{\Lambda}^{(n)}_{k_1\cdots k_n} = \frac{\alpha^{(n)}}{n}\sum_{p=1}^{n}\left(\frac{1}{\lambda_{k_p}}\prod_{m=1}^{n}\lambda_{k_m}\right)\int\left(\prod_{r=1}^{n}\phi^{k_r}\right)ds. \tag{A14}$$

Thus, the EFD approach provides a very simple expression for the classical solution for the amplitudes a_k

$$\mathbf{\Lambda} a_k = \left[j_k - \sum_{n=1}^{\infty}\frac{1}{n!}\sum_{k_1}^{K}\cdots\sum_{k_n}^{K}\tilde{\Lambda}^{(n+1)}_{k_1\cdots k_n}a_{k_1}\cdots a_{k_n}\right] \tag{A15}$$

through the eigenvalues and eigenvectors of the coupling matrix [that may also include some noise corrections (Frank and Galinsky 2016a,b)].

REFERENCES

Adlerman, E. J., K. K. Droegemeier, and R. Davies-Jones, 1999: A numerical simulation of cyclic mesocyclogenesis. *J. Atmos. Sci.*, **56**, 2045–2069, https://doi.org/10.1175/1520-0469(1999)056<2045:ANSOCM>2.0.CO;2.

Atkins, N. T., A. McGee, R. Ducharme, R. M. Wakimoto, and J. Wurman, 2012: The LaGrange tornado during VORTEX2. Part II: Photogrammetric analysis of the tornado combined with dual-Doppler radar data. *Mon. Wea. Rev.*, **140**, 2939–2958, https://doi.org/10.1175/MWR-D-11-00285.1.

Beck, J. R., J. L. Schroeder, and J. M. Wurman, 2006: High-resolution dual-Doppler analyses of the 29 May 2001 Kress, Texas, cyclic supercell. *Mon. Wea. Rev.*, **134**, 3125–3148, https://doi.org/10.1175/MWR3246.1.

Beckmann, C. F., and S. M. Smith, 2004: Probabilistic independent component analysis for functional magnetic resonance imaging. *IEEE Trans. Med. Imaging*, **23**, 137–152, https://doi.org/10.1109/TMI.2003.822821.

Bell, A. J., and T. J. Sejnowski, 1995: An information maximization approach to blind separation and blind deconvolution. *Neural Comput.*, **7**, 1129–1159, https://doi.org/10.1162/neco.1995.7.6.1129.

Bluestein, H. B., 2007: Advances in applications of the physics of fluids to severe weather systems. *Rep. Prog. Phys.*, **70**, 1259–1323, https://doi.org/10.1088/0034-4885/70/8/R01.

Brandes, E. A., 1978: Mesocyclone evolution and tornadogenesis: Some observations. *Mon. Wea. Rev.*, **106**, 995–1011, https://doi.org/10.1175/1520-0493(1978)106<0995:MEATSO>2.0.CO;2.

——, 1984: Vertical vorticity generation and mesocyclone sustenance in tornadic thunderstorms: The observational evidence. *Mon. Wea. Rev.*, **112**, 2253–2269, https://doi.org/10.1175/1520-0493(1984)112<2253:VVGAMS>2.0.CO;2.

Bryan, G. H., and J. M. Fritsch, 2002: A benchmark simulation for moist nonhydrostatic numerical models. *Mon. Wea. Rev.*, **130**, 2917–2928, https://doi.org/10.1175/1520-0493(2002)130<2917:ABSFMN>2.0.CO;2.

Burda, Z., J. Duda, J. M. Luck, and B. Waclaw, 2009: Localization of the maximal entropy random walk. *Phys. Rev. Lett.*, **102**, 160602, https://doi.org/10.1103/PhysRevLett.102.160602.

Burgers, J., 1948: A mathematical model illustrating the theory of turbulence. *Adv. Appl. Mech.*, **1**, 171–199, https://doi.org/10.1016/S0065-2156(08)70100-5.

Coffer, B. E., and M. D. Parker, 2017: Simulated supercells in nontornadic and tornadic VORTEX2 environments. *Mon. Wea. Rev.*, **145**, 149–180, https://doi.org/10.1175/MWR-D-16-0226.1.

Comon, P., 1994: Independent component analysis, A new concept? *Signal Processing*, **36**, 287–314, https://doi.org/10.1016/0165-1684(94)90029-9.

Craddock, J. M., 1973: Problems and prospects for eigenvector analysis in meteorology. *Statistician*, **22**, 133–145, https://doi.org/10.2307/2987365.

Dahl, J. M. L., M. D. Parker, and L. J. Wicker, 2012: Uncertainties in trajectory calculations within near-surface mesocyclones of simulated supercells. *Mon. Wea. Rev.*, **140**, 2959–2966, https://doi.org/10.1175/MWR-D-12-00131.1.

Davies-Jones, R., R. J. Trapp, and H. B. Bluestein, 2001: *Tornadoes and Tornadic Storms. Meteor. Monogr.*, No. 50, Amer. Meteor. Soc., 167–221, https://doi.org/10.1175/0065-9401-28.50.167.

Dowell, D. C., and H. B. Bluestein, 1997: The Arcadia, Oklahoma, storm of 17 May 1981: Analysis of a supercell during tornadogenesis. *Mon. Wea. Rev.*, **125**, 2562–2582, https://doi.org/10.1175/1520-0493(1997)125<2562:TAOSOM>2.0.CO;2.

——, and ——, 2002a: The 8 June 1995 McLean, Texas, storm. Part I: Observations of cyclic tornadogenesis. *Mon. Wea. Rev.*, **130**, 2626–2648, https://doi.org/10.1175/1520-0493(2002)130<2626:TJMTSP>2.0.CO;2.

——, and ——, 2002b: The 8 June 1995 McLean, Texas, storm. Part II: Cyclic tornado formation, maintenance, and dissipation. *Mon. Wea. Rev.*, **130**, 2649–2670, https://doi.org/10.1175/1520-0493(2002)130<2649:TJMTSP>2.0.CO;2.

Enßlin, T. A., M. Frommert, and F. S. Kitaura, 2009: Information field theory for cosmological perturbation reconstruction and nonlinear signal analysis. *Phys. Rev.*, **80D**, 105005, https://doi.org/10.1103/PhysRevD.80.105005.

Feynman, R. P., 1949: Space-time approach to quantum electrodynamics. *Phys. Rev.*, **76**, 769–789, https://doi.org/10.1103/PhysRev.76.769.

Frank, L. R., and V. L. Galinsky, 2014: Information pathways in a disordered lattice. *Phys. Rev.*, **89E**, 032142, https://doi.org/10.1103/PhysRevE.89.032142.

——, and ——, 2016a: Detecting spatio-temporal modes in multivariate data by entropy field decomposition. *J. Phys.*, **49A**, 395001, https://doi.org/10.1088/1751-8113/49/39/395001.

——, and ——, 2016b: Dynamic multiscale modes of resting state brain activity detected by entropy field decomposition. *Neural Comput.*, **28**, 1769–1811, https://doi.org/10.1162/NECO_a_00871.

——, R. B. Buxton, and E. C. Wong, 1998: Probabilistic analysis of functional magnetic resonance imaging data. *Magn. Reson. Med.*, **39**, 132–148, https://doi.org/10.1002/mrm.1910390120.

——, ——, and ——, 2001: Estimation of respiration-induced noise fluctuations from undersampled fMRI data. *Magn. Reson. Med.*, **45**, 635–644, https://doi.org/10.1002/mrm.1086.

French, M. M., P. S. Skinner, L. J. Wicker, and H. B. Bluestein, 2015: Documenting a rare tornado merger observed in the 24 May 2011 El Reno–Piedmont, Oklahoma, supercell. *Mon. Wea. Rev.*, **143**, 3025–3043, https://doi.org/10.1175/MWR-D-14-00349.1.

Galinsky, V. L., and L. R. Frank, 2015: Simultaneous multi-scale diffusion estimation and tractography guided by entropy spectrum pathways. *IEEE Trans. Med. Imaging*, **34**, 1177–1193, https://doi.org/10.1109/TMI.2014.2380812.

Grzych, M. L., B. D. Lee, and C. A. Finley, 2007: Thermodynamic analysis of supercell rear-flank downdrafts from Project ANSWERS. *Mon. Wea. Rev.*, **135**, 240–246, https://doi.org/10.1175/MWR3288.1.

Houser, J. L., H. B. Bluestein, and J. C. Snyder, 2015: Rapid-scan, polarimetric, Doppler radar observations of tornadogenesis and tornado dissipation in a tornadic supercell: The El Reno, Oklahoma storm of 24 May 2011. *Mon. Wea. Rev.*, **143**, 2685–2710, https://doi.org/10.1175/MWR-D-14-00253.1.

Jaynes, E. T., 1957a: Information theory and statistical mechanics. *Phys. Rev.*, **106**, 620–630, https://doi.org/10.1103/PhysRev.106.620.

——, 1957b: Information theory and statistical mechanics. II. *Phys. Rev.*, **108**, 171, https://doi.org/10.1103/PhysRev.108.171.

Klemp, J., and R. Rotunno, 1983: A study of the tornadic region within a supercell thunderstorm. *J. Atmos. Sci.*, **40**, 359–377, https://doi.org/10.1175/1520-0469(1983)040<0359:ASOTTR>2.0.CO;2.

Kosiba, K. A., and J. Wurman, 2013: The three-dimensional structure and evolution of a tornado boundary layer. *Wea. Forecasting*, **28**, 1552–1561, https://doi.org/10.1175/WAF-D-13-00070.1.

——, ——, Y. Richardson, P. Markowski, P. Robinson, and J. Marquis, 2013: Genesis of the Goshen County, Wyoming, tornado on 5 June 2009 during VORTEX2. *Mon. Wea. Rev.*, **141**, 1157–1181, https://doi.org/10.1175/MWR-D-12-00056.1.

Lorenz, E. N., 1956: Empirical orthogonal functions and statistical weather prediction. MIT Dept. of Meteorology Scientific Rep. 1, Statistical Forecasting Project, 52 pp., http://www.o3d.org/abracco/Atlantic/Lorenz1956.pdf.

Majcen, M., P. Markowski, Y. Richardson, D. Dowell, and J. Wurman, 2008: Multipass objective analyses of Doppler radar data. *J. Atmos. Oceanic Technol.*, **25**, 1845–1858, https://doi.org/10.1175/2008JTECHA1089.1.

Markowski, P. M., and Y. P. Richardson, 2009: Tornadogenesis: Our current understanding, forecasting considerations, and questions to guide future research. *Atmos. Res.*, **93**, 3–10, https://doi.org/10.1016/j.atmosres.2008.09.015.

——, and ——, 2014: The influence of environmental low-level shear and cold pools on tornadogenesis: Insights from idealized simulations. *J. Atmos. Sci.*, **71**, 243–275, https://doi.org/10.1175/JAS-D-13-0159.1.

——, J. M. Straka, and E. N. Rasmussen, 2002: Direct surface thermodynamic observations within the rear-flank downdrafts of nontornadic and tornadic supercells. *Mon. Wea. Rev.*, **130**, 1692–1721, https://doi.org/10.1175/1520-0493(2002)130<1692:DSTOWT>2.0.CO;2.

——, ——, and ——, 2003: Tornadogenesis resulting from the transport of circulation by a downdraft: Idealized numerical simulations. *J. Atmos. Sci.*, **60**, 795–823, https://doi.org/10.1175/1520-0469(2003)060<0795:TRFTTO>2.0.CO;2.

——, and Coauthors, 2012a: The pretornadic phase of the Goshen County, Wyoming, supercell of 5 June 2009 intercepted by VORTEX2. Part I: Evolution of kinematic and surface thermodynamic fields. *Mon. Wea. Rev.*, **140**, 2887–2915, https://doi.org/10.1175/MWR-D-11-00336.1.

——, and Coauthors, 2012b: The pretornadic phase of the Goshen County, Wyoming, supercell of 5 June 2009 intercepted by VORTEX2. Part II: Intensification of low-level rotation. *Mon. Wea. Rev.*, **140**, 2916–2938, https://doi.org/10.1175/MWR-D-11-00337.1.

Marquis, J. N., Y. P. Richardson, J. M. Wurman, and P. M. Markowski, 2008: Single- and dual-Doppler analysis of a tornadic vortex and surrounding storm scale flow in the Crowell, Texas, supercell of 30 April 2000. *Mon. Wea. Rev.*, **136**, 5017–5043, https://doi.org/10.1175/2008MWR2442.1.

——, ——, P. M. Markowski, D. Dowell, and J. M. Wurman, 2012: Tornado maintenance investigated with high-resolution dual-Doppler and EnKF analysis. *Mon. Wea. Rev.*, **140**, 3–27, https://doi.org/10.1175/MWR-D-11-00025.1.

——, ——, ——, ——, K. Kosiba, P. Robinson, and G. Romine, 2014: An investigation of the Goshen County, Wyoming, tornadic supercell of 5 June 2009 using EnKF assimilation of mobile mesonet and radar observations collected during VORTEX2. Part I: Experiment design and verification of the EnKF analyses. *Mon. Wea. Rev.*, **142**, 530–554, https://doi.org/10.1175/MWR-D-13-00007.1.

McKeown, M. J., S. Makeig, G. G. Brown, T. P. Jung, S. S. Kindermann, A. J. Bell, and T. J. Sejnowski, 1998: Analysis of fMRI data by blind separation into independent spatial components. *Science*, **6**, 160–188.

Obukhov, A. M., 1947: Statistically homogeneous fields on a sphere. *Usp. Mat. Nauk*, **2**, 196–198.

——, 1960: The statistically orthogonal expansion of empirical functions. *Izv. Akad. Nauk SSSR, Ser. Geofiz.*, **3**, 432–439.

Orf, L., R. Wilhelmson, B. Lee, C. Finley, and A. Houston, 2017: Evolution of a long-track violent tornado within a simulated supercell. *Bull. Amer. Meteor. Soc.*, **98**, 45–68, https://doi.org/10.1175/BAMS-D-15-00073.1.

Poline, J.-B., and M. Brett, 2012: The general linear model and fMRI: Does love last forever? *Neuroimage*, **62**, 871–880, https://doi.org/10.1016/j.neuroimage.2012.01.133.

Rotunno, R., and J. Klemp, 1985: On the rotation and propagation of simulated supercell thunderstorms. *J. Atmos. Sci.*, **42**, 271–292, https://doi.org/10.1175/1520-0469(1985)042<0271:OTRAPO>2.0.CO;2.

Ryder, L., 1985: *Quantum Field Theory*. 1st ed. Cambridge University Press, 508 pp.

Snyder, C., and F. Zhang, 2003: Assimilation of simulated Doppler radar observations with an ensemble Kalman filter. *Mon. Wea. Rev.*, **131**, 1663–1677, https://doi.org/10.1175//2555.1.

Tanamachi, R. L., P. L. Heinselman, and L. J. Wicker, 2015: Impacts of a storm merger on the 24 May 2011 El Reno, Oklahoma, tornadic supercell. *Wea. Forecasting*, **30**, 501–524, https://doi.org/10.1175/WAF-D-14-00164.1.

Thompson, R. L., R. Edwards, J. A. Hart, K. L. Elmore, and P. Markowski, 2003: Close proximity soundings within supercell environments obtained from the Rapid Update Cycle. *Wea. Forecasting*, **18**, 1243–1261, https://doi.org/10.1175/1520-0434(2003)018<1243:CPSWSE>2.0.CO;2.

Trapp, R. J., 1999: Observations of nontornadic low-level mesocyclones and attendant tornadogenesis failure during VORTEX. *Mon. Wea. Rev.*, **127**, 1693–1705, https://doi.org/10.1175/1520-0493(1999)127<1693:OONLLM>2.0.CO;2.

Tryggeson, H., 2007: Analytical vortex solutions to the Navier-Stokes equation. Acta Wexionensia, No. 114/2007, Växjö University, 108 pp., https://www.diva-portal.org/smash/get/diva2:205082/FULLTEXT01.pdf.

Wakimoto, R. M., and H. Cai, 2000: Analysis of a nontornadic storm during VORTEX 95. *Mon. Wea. Rev.*, **128**, 565–592, https://doi.org/10.1175/1520-0493(2000)128<0565:AOANSD>2.0.CO;2.

——, N. T. Atkins, and J. Wurman, 2011: The LaGrange tornado during VORTEX2. Part I: Photogrammetric analysis of the tornado combined with single-Doppler radar data. *Mon. Wea. Rev.*, **139**, 2233–2258, https://doi.org/10.1175/2010MWR3568.1.

——, P. Stauffer, W.-C. Lee, N. T. Atkins, and J. Wurman, 2012: Finescale structure of the LaGrange, Wyoming, tornado during VORTEX2: GBVTD and photogrammetric analyses. *Mon. Wea. Rev.*, **140**, 3397–3418, https://doi.org/10.1175/MWR-D-12-00036.1.

Wicker, L. J., and R. B. Wilhelmson, 1995: Simulation and analysis of tornado development and decay within a three-dimensional supercell thunderstorm. *J. Atmos. Sci.*, **52**, 2675–2703, https://doi.org/10.1175/1520-0469(1995)052<2675:SAAOTD>2.0.CO;2.

Woolrich, M. W., M. Jenkinson, J. M. Brady, and S. M. Smith, 2004: Fully Bayesian spatio-temporal modeling of FMRI data. *IEEE Trans. Med. Imaging*, **23**, 213–231, https://doi.org/10.1109/TMI.2003.823065.

Wurman, J., 2001: The DOW mobile multiple Doppler network. Preprints, *30th Conf. on Radar Meteorology*, Munich, Germany, Amer. Meteor. Soc., 95–97.

——, and K. A. Kosiba, 2013: Finescale radar observations of tornado and mesocyclone structures. *Wea. Forecasting*, **28**, 1157–1174, https://doi.org/10.1175/WAF-D-12-00127.1.

——, J. Straka, E. Rasmussen, M. Randall, and A. Zahrai, 1997: Design and deployment of a portable, pencil-beam, pulsed, 3-cm Doppler radar. *J. Atmos. Oceanic Technol.*, **14**, 1502–1512, https://doi.org/10.1175/1520-0426(1997)014<1502:DADOAP>2.0.CO;2.

——, Y. Richardson, C. Alexander, S. Weygandt, and P. F. Zhang, 2007a: Dual-Doppler analysis of winds and vorticity budget terms near a tornado. *Mon. Wea. Rev.*, **135**, 2392–2405, https://doi.org/10.1175/MWR3404.1.

——, ——, ——, ——, and ——, 2007b: Dual-Doppler and single-Doppler analysis of a tornadic storm undergoing mergers and repeated tornadogenesis. *Mon. Wea. Rev.*, **135**, 736–758, https://doi.org/10.1175/MWR3276.1.

——, P. Robinson, C. Alexander, and Y. Richardson, 2007c: Low-level winds in tornadoes and potential catastrophic tornado impacts in urban areas. *Bull. Amer. Meteor. Soc.*, **88**, 31–46, https://doi.org/10.1175/BAMS-88-1-31.

——, K. A. Kosiba, P. Markowski, Y. Richardson, D. Dowell, and P. Robinson, 2010: Finescale single-and dual-Doppler analysis of tornado intensification, maintenance, and dissipation in the Orleans, Nebraska, supercell. *Mon. Wea. Rev.*, **138**, 4439–4455, https://doi.org/10.1175/2010MWR3330.1.

——, D. Dowell, Y. Richardson, P. Markowski, E. Rasmussen, D. Burgess, L. Wicker, and H. B. Bluestein, 2012: The second Verification of the Origins of Rotation in Tornadoes Experiment: VORTEX2. *Bull. Amer. Meteor. Soc.*, **93**, 1147–1170, https://doi.org/10.1175/BAMS-D-11-00010.1.

——, K. Kosiba, P. Robinson, and T. Marshall, 2014: The role of multiple-vortex tornado structure in causing storm researcher fatalities. *Bull. Amer. Meteor. Soc.*, **95**, 31–45, https://doi.org/10.1175/BAMS-D-13-00221.1.